mathematics

MDPI

Article

Computational Method for Dynamic Analysis of Multibody Systems with Deformable Elements

Sorin Dumitru, Nicolae Dumitru *, Cristian Copilusi and Adrian Sorin Rosca

Faculty of Mechanics, University of Craiova, 200585 Craiova, Romania; sorin.dumitru@edu.ucv.ro (S.D.); cristian.copilusi@edu.ucv.ro (C.C.); sorin.rosca@edu.ucv.ro (A.S.R.)
* Correspondence: nicolae.dumitru@edu.ucv.ro; Tel.: +40-740-084-392

Abstract

The dynamics of mechanical systems with fast motions and dynamic loads are strongly influenced by the deformability of kinematic elements. The finite element method and the superposition of rigid body motion with deformable body motion allow us to determine a new structure for the matrices that define the mechanical system equations of motion. Meshing the kinematic elements into finite elements causes the unknowns of the problem to no longer be displacement functions but rather nodal displacements. These displacements are considered as a linear combination of modal shapes and modal coordinates. This method is applied to a drive mechanism of an internal combustion engine with three pistons mounted in line. The system is driven by the pressure exerted by the gas on the piston head, which was experimentally determined. The longitudinal and transversal deformations of the connecting rod are determined, including the nodal displacements. These results were verified through virtual prototyping on the 3D model, using multibody system theory and the finite element method. The recorded differences are mainly explained by the type, size, and shape of the used finite elements. Experimental analysis allows us to determine the connecting rod kinematic and dynamic parameters as functions of time and frequency variation. The developed method is flexible and can be easily adapted to systems with fast motions in which, during operation, impact forces appear in joints for various reasons.

Keywords: finite element; dynamic analysis; deformable bodies; vibration modes; engine mechanism; joint clearance

MSC: 74-101

check for updates

Academic Editors: Alicia Cordero and Xiangmin Jiao

Received: 4 July 2025
Revised: 24 August 2025
Accepted: 27 August 2025
Published: 31 August 2025

Citation: Dumitru, S.; Dumitru, N.; Copilusi, C.; Rosca, A.S. Computational Method for Dynamic Analysis of Multibody Systems with Deformable Elements. *Mathematics* **2025**, *13*, 2797. https://doi.org/10.3390/math13172797

Copyright: © 2025 by the authors. Licensee MDPI, Basel, Switzerland. This article is an open access article distributed under the terms and conditions of the Creative Commons Attribution (CC BY) license (https://creativecommons.org/licenses/by/4.0/).

1. Introduction

The elasto-dynamic analysis of mobile mechanical systems is an area of ongoing research, particularly regarding the dynamics of such systems that include elastic components. Research in this field focuses on accurately modeling the vibrations and flexibility of the components within the structure of the studied mechanism, as well as experimentally validating the results; see [1,2].

Surveys and studies on mobile mechanical systems have facilitated the analysis of elasto-dynamic phenomena and vibrations during high-speed operating conditions. The finite element method is used in these analyses to provide a detailed representation of deformations, fully integrated with the kinematic and dynamic models of the mechanisms under investigation. Additionally, theoretical research is complemented by experimental

validations, allowing for direct comparison with simulations and numerical processing, as described in [3,4].

Regarding elasto-dynamic analysis, an integrated approach involving theoretical (mathematical) modeling, numerical processing, virtual prototyping, and experimental validation, as described in [5], provides methodological extensibility for mobile mechanical systems. This approach aligns with established formalisms such as those proposed by Lagrange, Gibbs–Appell, and Hamilton. When integrated with the finite element method or multibody dynamics, it contributes to contemporary research initiatives focused on maintaining continuity within this field of research.

Conversely, [6–8], which employ the previously mentioned approach, are highly complex due to their use of the finite element method and comparison of the modal dynamic analysis results. If we refer to [6], it can be observed that the Gibbs–Appell method provides better results than the Lagrange method. Thus, the Gibbs–Appell method is applied instead of Lagrange's equations, starting from the acceleration energy in order to obtain the equations of motion. The numerical processing of the developed mathematical model was compared with a model analyzed using the finite element method, in which voids were inserted at 1%, 2%, 3%, and 4% by randomly removing elements from the mesh. The conclusion reached is that even with 4% voids, the influence of vibrations is negligible, but the maximum stresses increase visibly, and the internal displacements vary. Moreover, the concept of acceleration energy is less known among engineers compared to the kinetic and potential energy used in the Lagrange method, with few concrete applications—but with clear potential in the context of complex system dynamics. This research is also referenced in the review presented in [7], which introduces a unified framework for differentiating the equations of motion for a mechanical system using different theoretical methods: Lagrange, Gibbs–Appell, Kane, Maggi, and Hamilton. These theoretical methods are applied in the context of 2D modeling using FEM, combined with dynamic formulations. The aim of this research is to highlight a rigorous comparative approach to the formulations in analytical mechanics applied to the modeling of flexible multibody systems in a two-dimensional plane. By evaluating the advantages and limitations of each formalism (Lagrange, Gibbs–Appell, Kane, Maggi, Hamilton), the authors emphasize the potential of more efficient methods—such as Gibbs–Appell or Maggi—in reducing computational cost while preserving the accuracy of the 2D FEM system dynamics. Also included in this category is the research presented in [8], where a powerful and efficient method is demonstrated for modeling cooperative robotic systems composed of mobile robots with flexible arms, using recursive Gibbs–Appell formulation. The advantages are clear: the elegant handling of constraints, reduced symbolic complexity, and strong potential for application in complex systems, from industrial robotics to precise cooperative manipulation.

Such approaches involve a large volume of numerical processing and entail lengthy computation times, especially for extended models. Additionally, the validation of the methods and tools specific to elasto-dynamic analysis is a critical consideration. In these cases, validation was performed on a single mechanism, using a limited validation approach. Consequently, validating other mechanism configurations requires adapting the methods and newly validating the undertaken research.

According to the findings presented in [9,10], measurement errors and inconsistencies are significant factors that affect experimental outcomes. It becomes evident that such determinations are susceptible to vibrations and varying experimental conditions. As a result, the results reveal incomplete alignments or discrepancies compared to the numerical processing of the mathematical models and results derived from virtual prototyping.

Moreover, the research presented in [10] addresses another critical aspect of the dynamic behavior of mobile mechanical systems: the presence of mechanical clearance in

the kinematic joints of spatial mechanisms. The analysis focuses on the advanced dynamic modeling of a spatial mechanism that includes impact forces and friction within the joints, specifically adapted for microgravity conditions. The experimental component prioritizes the effects of joint clearance, which can notably diminish motion accuracy under microgravity conditions. It is also noted that the analytical methods applied to the mechanism's dynamics have limited scope, and expanding their applicability to more complex mechanisms will require significant modifications.

Similarly to [10], the research carried out in [11] also highlights several study methods applied to planar mechanisms but with ambiguous experimental validation, which can only be certified through virtual prototyping.

A key factor in the elasto-dynamic analysis of mobile mechanical systems is the reliance on the mechanical properties of the materials that comprise the system's components. Previous research, such as [12,13], has examined components constructed from materials exhibiting linear elasticity. However, ongoing studies are now focusing on elasto-dynamic analysis for mobile mechanical systems with significant component deformations or materials with nonlinear mechanical properties, as outlined in [14–16].

In [17], the authors introduced a hybrid elasto-dynamic modeling approach in which the mobile mechanical system is divided into substructures; specific segments are analyzed numerically, while others are examined through experimental testing. The comprehensive model of the system is constructed using frequency-based substructuring methods. The objective of this research is to enhance the accuracy of predictions related to vibrations, system stability, and dynamic loads. Consequently, the methodology employs complex numerical modeling combined with experimental validation, employing rigorous procedures to minimize potential errors and ensure the reliability of the results.

Under specific circumstances, the novel component that underpins current elasto-dynamic investigations on mobile mechanical systems is linked to the development of mathematical models aimed at understanding the impact forces within joints and potential deviations. These deviations significantly influence the quality of the results, which are rigorously validated, especially from an experimental viewpoint, as endorsed in [18–20].

The main objectives set for the present research study are outlined below.

We aim at the development of a computational method used in the dynamic analysis of mechanisms with deformable elements. For our research, we employed the finite element method to analyze the dynamics of a mechanism within an internal combustion engine that features deformable kinematic components. Next, we developed a comparative study of the results obtained following our close mathematical model processing, virtual prototyping, and experimental analysis of the mechanism.

The novelty in this is represented by the use of the finite element method in the dynamics of mobile mechanical systems and in replacing the continuous system with a discrete one with a finite number of degrees of freedom. Additionally, by superimposing the motion of the rigid body with that of the deformable body, the static and dynamic components of the matrices that define the equations of motion were identified. As a result, the unknowns of the problem became the nodal coordinates. The multibody system is considered as an assembly composed of finite elements connected through nodes or as substructures. These substructures are subjected to the constraint forces from the kinematic joints. Therefore, compared to other methods, it is possible to take into account the dynamic loads within the joints, such as impact forces, for example. In the same context, the developed dynamic model can also be used for kinematic elements made of materials with nonlinear behavior.

The proposed research workflow is schematized in Figure 1.

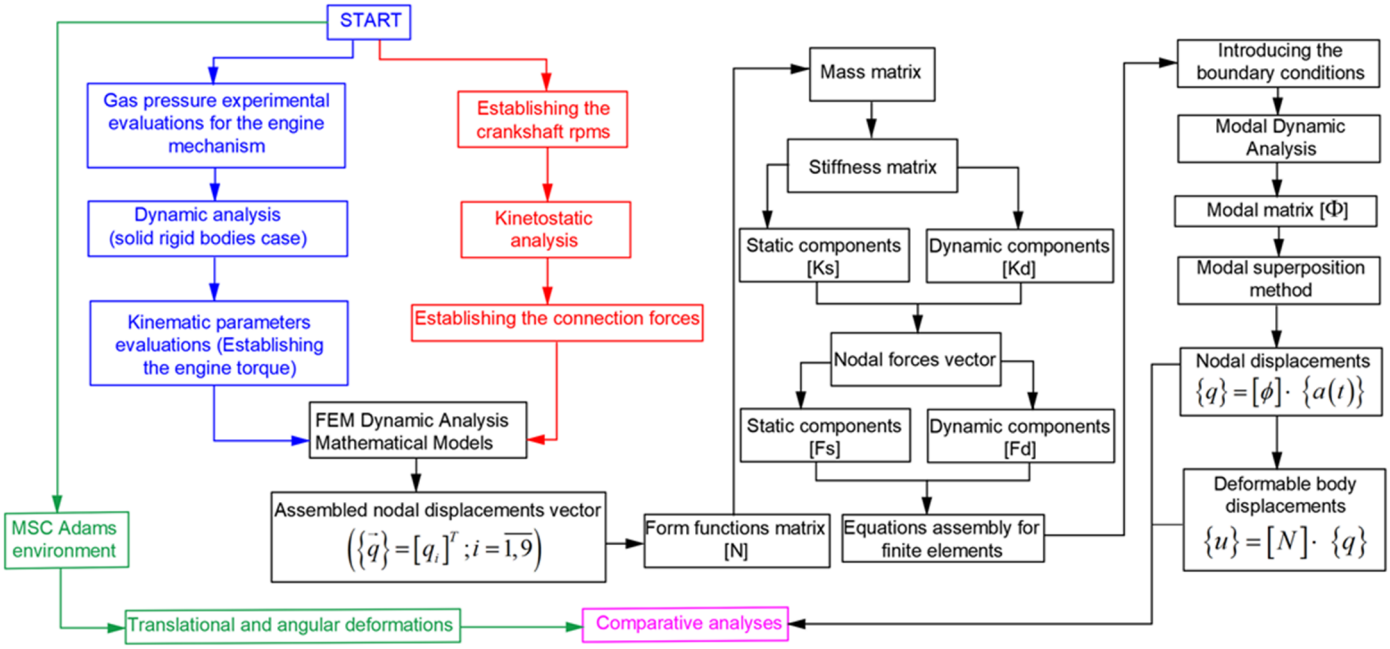


Figure 1. Research workflow.

The key contributions of our study are outlined below, as indicated in Figure 1:

We built a dynamic model of the equations of motion via the finite element method as applied to a complex mechanism with fast movements under dynamic loads; we decoupled the equations of motion and processed mathematical models for dynamic modal analysis; we conducted a time-dependent experimental study of the force exerted by gas on the piston; we performed the virtual prototyping of the mechanism's dynamics and the identification of the time variation function of motor torque; and we created an algorithm and a program outline for the dynamic modal analysis of mechanisms with deformable elements.

2. Mathematical Models for Dynamic Analysis of Mechanisms with Deformable Elements

A kinematic linkage consisting of "$n-1$" rigid solids connected by kinematic joints is shown in Figure 2. In this case, solid "n" is considered to be a deformable body.

The following notations are introduced:

$R_i\left(\vec{x}_i, \vec{y}_i, \vec{z}_i\right)$ is the reference coordinate system attached to the link "i" with a versor base of $W_i\left(\vec{i}_i, \vec{j}_i, \vec{k}_i\right)$.

$R_0\left(\vec{x}_0, \vec{y}_0, \vec{z}_0\right)$ is the global reference coordinate system with a versor base of $W_0\left(\vec{i}_0, \vec{j}_0, \vec{k}_0\right)$.

$\vec{\delta}_i$ is the relative translational vector between "i" and "$i-1$", depending on "$Ri-1$", which exists if there is a joint between the "i" and "$i-1$" links.

$\bar{r}_i$—position vector of the "$O'i$" point, expressed in the "$Ri-1$" reference coordinate system, when the relative translation begins.

Thus, the following equations can be written:

$$\vec{\delta}_i = \left\{\delta_i^x, \delta_i^y, \delta_i^z\right\}_{i-1} = \{\delta_i\}^T \left\{\vec{W}_{i-1}\right\} \quad (1)$$

$$\vec{\delta}_i = \left\{\delta_i^x, \delta_i^y, \delta_i^z\right\}_{i-1} = \{\delta_i\}^T \left\{\vec{W}_{i-1}\right\} \quad (2)$$

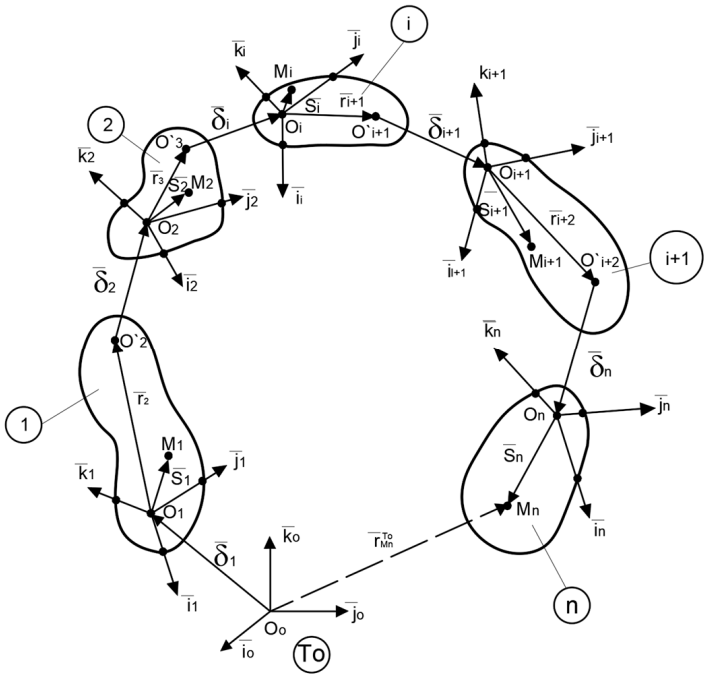


Figure 2. General kinematic model.

Transformation matrices for converting between reference coordinate systems are then introduced, as seen in Equation (3).

$$\left\{\vec{W}_{i-1}\right\} = [A_{0i-1}]\left\{\vec{W}_0\right\} \tag{3}$$

Thus, Equations (1) and (2) become the following:

$$\overline{r_i} = \{r_i\}^T\left\{\vec{W}_{i-1}\right\} = \{r_i\}^T[A_{0i-1}]\left\{\vec{W}_0\right\} \tag{4}$$

$$\vec{\delta_i} = \{\delta_i\}^T\left\{\vec{W}_{i-1}\right\} = \{\delta_i\}^T[A_{0i-1}]\left\{\vec{W}_0\right\} \tag{5}$$

Referring to Figure 3, on the "*En*" link, the "*Mn*" point and the displacement $u(M,t)$ are considered. The position vector of point "*P*" is given by the following:

$$\vec{r} = \vec{r_{n-1}} + \vec{r_u} \tag{6}$$

$$\vec{r_u} = \vec{r_n} + \vec{u} \tag{7}$$

$$\vec{r_{n-1}} = \sum_{i=1}^{n}\left(\{r_i\}^T + \{\delta_i\}^T\right)[A_{0\,i-1}]\left\{\vec{W_0}\right\}, \tag{8}$$

where $[A_{0i-1}]$ represents the coordinate transformation matrix.

The elastic displacement vector is as follows:

$$\vec{u} = \{u\}^T\left\{\vec{w_n}\right\} \tag{9}$$

$$\{u\} = [N]\{q\}, \tag{10}$$

where $[N]$ represents the form function matrix or interpolating polynomial matrix; q is the nodal displacement vector.

$$\left\{\vec{w_n}\right\} = [A_{0,n}]\left\{\vec{w_0}\right\} \tag{11}$$

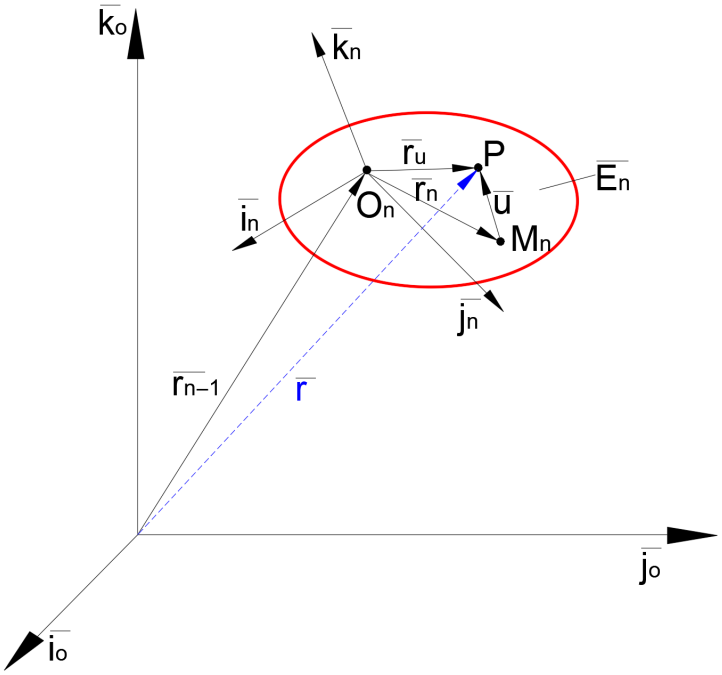


Figure 3. Geometrical model of elastic solid.

From the previous equations, we obtain the following:

$$\vec{u} = \{q\}^T [N]^T [A_{0,n}] \left\{ \vec{w_0} \right\} \tag{12}$$

$$\vec{r_n} = \{r_n\}^T \left\{ \vec{w_n} \right\} = \{r_n\}^T [A_{0,n}] \left\{ \vec{w_0} \right\} \tag{13}$$

$$\begin{aligned} \vec{r_u} &= \{r_n\}^T [A_{0,n}] \left\{ \vec{w_0} \right\} + \{q\}^T [N]^T [A_{0,n}] \left\{ \vec{w_0} \right\} = \\ &= \left(\{r_n\}^T + \{q\}^T [N]^T \right) [A_{0,n}] \left\{ \vec{w_0} \right\} \end{aligned} \tag{14}$$

Equations (8) and (14) are then incorporated into Equation (6) as follows:

$$\vec{r} = \left(\sum_{i=1}^{n} \left(\{r_i\}^T + \{\delta_i\}^T \right) [A_{0\,i-1}] + \left(\{r_n\}^T + \{q\}^T [N]^T \right) [A_{0,n}] \right) \left\{ \vec{w_0} \right\} \tag{15}$$

The following generalized coordinates are then taken into consideration:

$$\{p_i\}^T = \{\{r_i\} \ \{\delta_i\}\}^T \tag{16}$$

Thus, we obtain the following:

$$\vec{r} = \left(\sum_{i=1}^{n} \{p_i\}^T [A_{0\,i-1}] + \left(\{r_n\}^T + \{q\}^T [N]^T \right) [A_{0,n}] \right) \left\{ \vec{w_0} \right\} \tag{17}$$

To calculate speed, Equation (17) is differentiated relative to time:

$$\dot{\vec{r}} = \dot{\vec{r}}_{n-1} + \dot{\vec{r}}_u \tag{18}$$

Additionally, Equation (14) is differentiated relative to time, resulting in the following:

$$\dot{\vec{r}}_u = \dot{\vec{r}}_n + \dot{\vec{u}} = \dot{\vec{r}}_u + \frac{\partial u}{\partial t} + \vec{\omega} \times \vec{u} \tag{19}$$

By differentiating successively in rapport with the time of (15), and taking into account (17), the speeds and accelerations of the "P" point can be obtained: ($\vec{v} = \frac{d\vec{r}}{dt}$; $\vec{a} = \frac{d^2\vec{r}}{dt^2}$). Accordingly, the appropriate mathematical models for the equations of motion in Kane's formalism are developed for the holonomic case as follows [21]:

$$Q + Q^* = 0, \tag{20}$$

where Q represents the generalized forces associated with the exterior loadings and connection forces; Q* represents the generalized forces associated with inertial torsors.

$$Q = \sum_{k=1}^{p} \vec{F}_k \vec{v}_{rk} + \sum_{i=1}^{n} \vec{M}_i \vec{\omega}_{ri} \tag{21}$$

where $\vec{F}_k$ is the resultant force associated with the "M_k" point; $\vec{v}_{rk}$ is the partial speed related to $\vec{v}_k$, the speed of the "M_k" point; $\vec{M}_i$ is the resulting torque associated with the "i" kinematic element. $\vec{\omega}_{ri}$ is the partial angular speed, associated with the "i" element and the "v_r" generalized speed.

$$Q^* = \sum_{k=1}^{p} \vec{F}_{in_k} \vec{v}_k + \sum_{i=1}^{s} \vec{M}_{in} \vec{\omega}_{ri} + \sum_{i=1}^{s} \vec{F}_{in_i} \vec{v}_r \tag{22}$$

For the "i" element, considering the "q" nodal displacements, the generalized force related to the inertial torsors is expressed as follows:

$$Q_i^* = \vec{F}_{in_i} \frac{\partial \vec{v}_i}{\partial \dot{q}} + \vec{M}_{in_i} \frac{\partial \vec{\omega}_i}{\partial \dot{q}} \tag{23}$$

For the "i" element, the following notation may be used:

$$\vec{F}_{in_i} = -m_i \vec{a}_i \tag{24}$$

$$\vec{M}_{in_i} \frac{\partial \vec{\omega}_i}{\partial \dot{q}} \approx 0 \tag{25}$$

In (25), since the "ω" speed is small, it can be neglected.

According to the "P" point speed relation, we can obtain the following:

$$\frac{\partial \vec{v}}{\partial \dot{q}} = [N]^T [A_{0,n}] \left\{ \vec{w}_0 \right\} \tag{26}$$

The generalized force attached to the exterior forces, by additionally considering the stiffness and damping, is as follows:

$$Q = F_e - F_k - F_c \tag{27}$$

Considering the exterior forces and the exterior torque T, which actuates on the considered element, we obtain the following:

$$F_e = \vec{F} \frac{\partial \vec{v}}{\partial \dot{q}} + \vec{T} \frac{\partial \vec{\omega}}{\partial \dot{q}} = \vec{F} \frac{\partial \vec{v}}{\partial \dot{q}} \tag{28}$$

Thus, we consider the angular speed ω at small values, and we obtain the following: $\frac{\partial \vec{\omega}}{\partial \dot{q}} = 0$.

By considering F—the force that actuates on the "n" element—we obtain the following:

$$\vec{F} = \{F\}^T \left\{\vec{w_n}\right\} = \{F\}^T [A_{0,n}] \left\{\vec{w_0}\right\} \tag{29}$$

$$\vec{F_e} = \vec{F} \frac{\partial \vec{v}}{\partial \dot{q}} = \{F\}^T [N] \tag{30}$$

The force resulting from the "n" element stiffness [22] is as follows:

$$F_k = \{q\}^T [K] \tag{31}$$

where $[K]$ is the stiffness matrix [22], given by the following:

$$[K] = [B]^T [D][B] \tag{32}$$

In (32), we identify the following: $[B]$—the connection matrix between deformations and displacements and $[D]$—the material property matrix.

As a result, the force generated by damping can be expressed as follows:

$$F_c = \left\{\dot{q}\right\}^T [C], \tag{33}$$

where $[C]$ is the damping matrix [22] given by the following:

$$[C] = [N]^T [\mu]\, [N] \tag{34}$$

where $[\mu]$ is the damping coefficient matrix.

$$Q = F_e - F_k - F_c = \{F\}^T [N] - \{q\}^T [K] - \left\{\dot{q}\right\}^T [C] \tag{35}$$

Referring to Equation (20), where $Q + Q^* = 0$, and introducing Equation (35) in (20), we obtain the analytical expressions for the matrices that will define the equations of motion:

$$\begin{aligned} &\{F\}^T [N] - \{q\}^T [K] - \left\{\dot{q}\right\}^T [C] - m\left\{\sum_{i=1}^{n}\left(\left\{\ddot{p}_i\right\}^T [A_{0,i-1}][A_{0,n}]^T [N] + \right.\right. \\ &+2\left\{\dot{p}_i\right\}^T [\widetilde{\omega}_{0,i-1}][A_{0,i-1}][A_{0,n}]^T [N] + \{p_i\}^T [\widetilde{\varepsilon}_{0,i-1}][A_{0,i-1}][A_{0,n}]^T [N] + \\ &\left.\left.+\{p_i\}^T [\widetilde{\omega}_{0,i-1}][\widetilde{\omega}_{0,i-1}][A_{0,i-1}][A_{0,n}]^T [N]\right) + \left\{\ddot{q}\right\}^T [N]^T [N] + \right. \\ &+2\left\{\dot{q}\right\}^T [N]^T [\widetilde{\omega}_{0,n}][N] + \{r_n\}^T [\widetilde{\varepsilon}_{0,n}][N] + \{q\}^T [N]^T [\widetilde{\varepsilon}_{0,n}][N] + \\ &+\{r_n\}^T [\widetilde{\omega}_{0,n}][\widetilde{\omega}_{0,n}][N] + \{q\}^T [N]^T [\widetilde{\omega}_{0,n}][\widetilde{\omega}_{0,n}][N] = 0 \end{aligned} \tag{36}$$

The motion of a finite element "e" [23] is described by the following equation system:

$$\left\{\ddot{q}\right\}^T [M_e] + \left\{\dot{q}\right\}^T [C_e] + \{q\}^T [K_e] = [F_e]^T \tag{37}$$

From Equation (36), we identify the term coefficients $\left\{\ddot{q}\right\}^T$, $\left\{\dot{q}\right\}^T$, and $\{q\}^T$, namely $[M_e]$, $[C_e]$, and $[K_e]$, as follows:

The mass matrix is as follows:

$$\left[M^{(e)}\right] = \iiint_{V^{(e)}} \rho_e m_e [N]^T [N] dV \tag{38}$$

The damping matrix, including both static and dynamic components, is as follows:

$$[C^{(e)}] = \iiint\limits_{V^{(e)}} [N]^T[\mu][N]dV + 2\iiint\limits_{V^{(e)}} \rho_e[N]^T\left([\widetilde{\omega}_{0n}][\widetilde{\omega}_{0n}] + [\widetilde{\varepsilon}_{0n}]\right)[N]dV = [C_s^{(e)}] + [C_d^{(e)}] \quad (39)$$

The elemental nodal force can be determined with the following relation:

$$\begin{aligned}\left\{F^{(e)}\right\} = \iiint\limits_{V^{(e)}} \{N\}^T[F]dV - \iiint\limits_{V^{(e)}} \rho_e[N]^T\{([\widetilde{\varepsilon}_{0,n}] + [\widetilde{\omega}_{0,n}][\widetilde{\omega}_{0,n}])\{r_n\} + \\ + \sum_{i=1}^{n}[A_{n-1}]\left(\left\{\ddot{p}_i\right\} + 2[\widetilde{\omega}_{0,i-1}]\left\{\dot{p}_i\right\} + [\widetilde{\varepsilon}_{0,i-1}]\{p_i\} + [\widetilde{\omega}_{0,i-1}][\widetilde{\omega}_{0,i-1}]\{p_i\}\right)\}dV\end{aligned} \quad (40)$$

The stiffness matrix, which includes both static and dynamic components, is as follows:

$$[K^{(e)}] = \iiint\limits_{V^{(e)}} [B]^T[D][B]dV + \iiint\limits_{V^{(e)}} \rho_e[N]^T\left([\widetilde{\omega}_{0n}][\widetilde{\omega}_{0n}] + [\varepsilon_{0,n}]\right)[N]dV = [K_s^{(e)}] + [K_d^{(e)}] \quad (41)$$

3. An Elasto-Dynamic Analysis of the Mechanism from an Internal Combustion Engine

A mechanism from an internal combustion engine featuring three inline pistons, as illustrated in Figure 4b, will be examined in terms of both kinematic and dynamic characteristics. This mechanism consists of the following components: crankshaft 1, connecting rod 2, and piston 3. A kinematic diagram of the mechanism is shown in Figure 4a. Figure 4b shows the 3D model of the mechanism obtained through virtual prototyping. The analyzed motion is transmitted from the crankshaft via connecting rods to the three inline pistons. Understanding both the functional role and the mechanism usage, it is established that the operational cycle features rapid movements with pronounced dynamic characteristics. Consequently, it is essential to perform both kinematic and kinetostatic analyses, which require determining time-dependent motion laws for kinematic parameters, as well as evaluating the connection forces within the kinematic joints. The crankshaft rotational speed is 6000 rpm.

The mechanism's motion is tracked every 0.04 s during two complete crankshaft rotations.

Due to the rapid movement of the links, which generates significant inertial forces, an elasto-dynamic analysis of the mechanism is conducted. To achieve this, the connecting rods of the mechanism are considered deformable bodies.

For the inverse dynamic analysis, it is essential to have precise information regarding the crankshaft's angular velocity (ω = 628.318 radians/second), the crank slider length (r = 40 mm), and the connecting rod length (l = 137 mm), as well as the mass properties of the mechanism's links (m_1 = 0.952 kg; m_2 = 0.153 kg; and m_3 = 0.214 kg). Additionally, the gas pressure exerted on the piston head must be considered.

The force generated by the gas pressure acting upon the piston head is as follows:

$$F_g = p_g A_p, \quad (42)$$

where p_g—gas pressure, established experimentally; A_p—piston head surface.

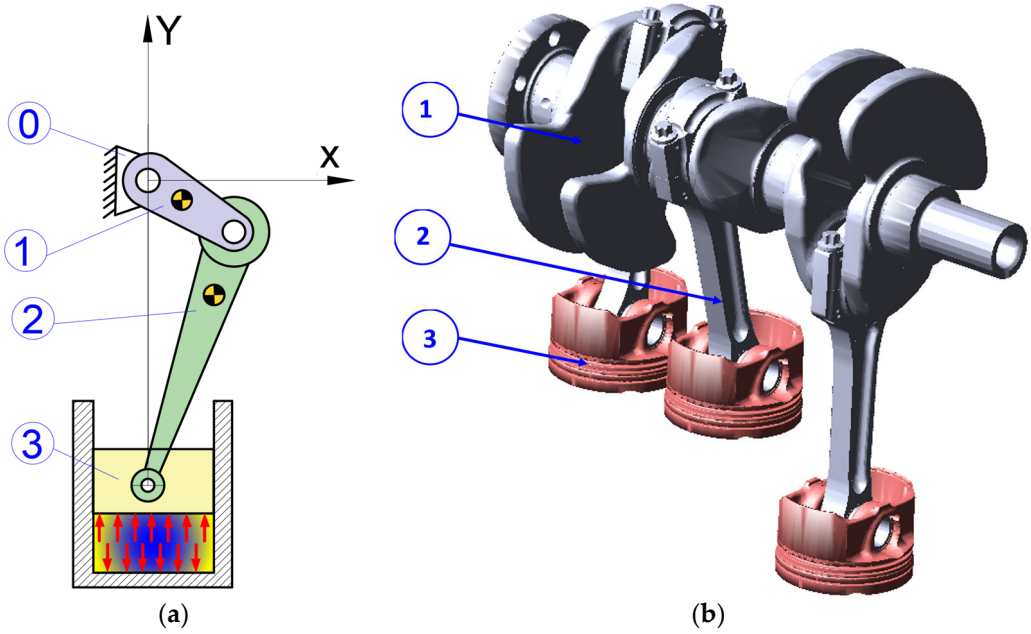


Figure 4. Internal combustion engine mechanism components (0—cylinder block, which is a fixed part; 1—crankshaft; 2—connecting rod; 3—piston). (**a**). Kinematic scheme. (**b**). Virtual model of internal combustion engine mechanism.

The gas pressure exerted on the piston head was experimentally measured as a function of the crankshaft angle, as illustrated in Figure 5.

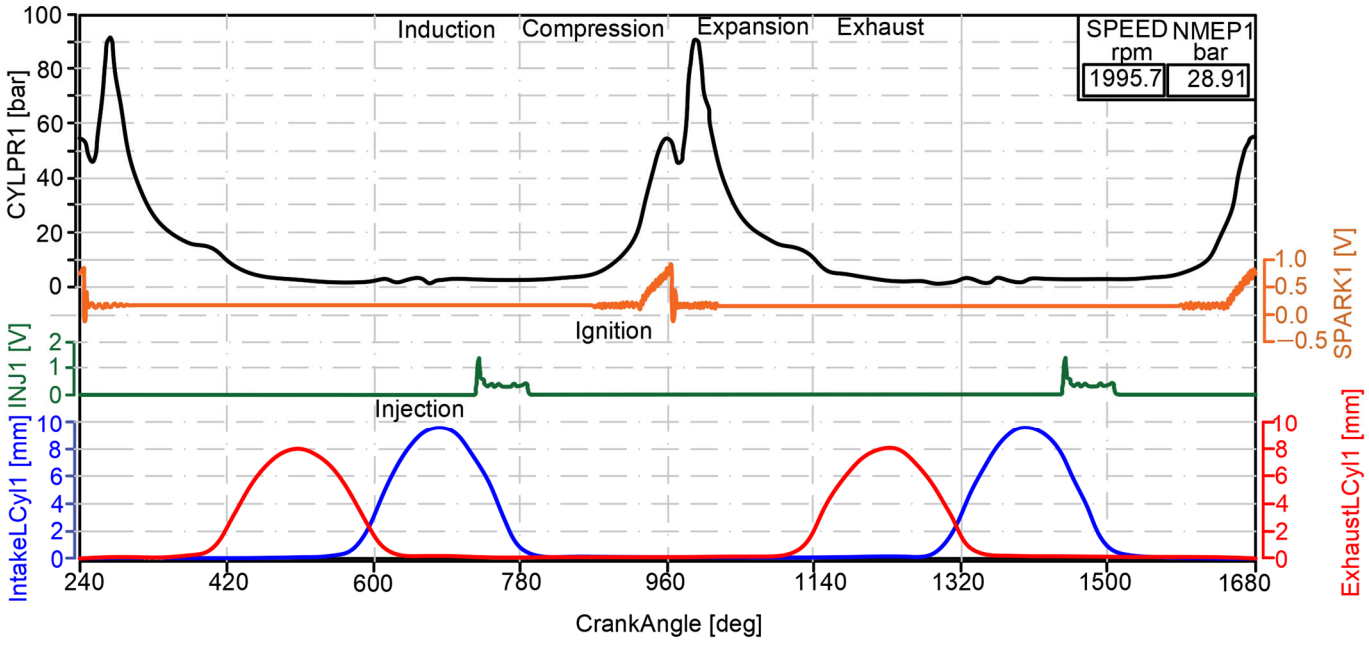


Figure 5. Variation in engine dynamic parameters depending on crankshaft rotation angle.

Figure 5 displays the main parameter variations in an internal combustion engine as a function of the crankshaft rotational angle (Crank Angle, degrees). The diagram illustrates the four distinct phases of the engine cycle: intake, compression, power, and exhaust. The key components shown in Figure 5 are as follows:

- Black curve (cylinder gas pressure): Two major peaks are visible, corresponding to successive combustion events. The maximum values exceed 90 bar, indicating the fuel

expansion phase. During compression, pressure increases before ignition, followed by a rapid drop after the exhaust phase.

- Orange curve (fuel ignition): This curve shows the exact ignition point of the fuel, correlated with the peak pressure. There is a measurable delay between injection and ignition that can be analyzed to improve engine performance.
- Green curve (reaction force in the piston, *Fx*): The force rises sharply at ignition and then gradually decreases. This pattern indicates that gas expansion produces a peak force on the piston, which affects the mechanical power output.

Red and blue curves (intake and exhaust valve lift): Intake valves (blue curve) open at the beginning of the intake stroke and close at its end. The exhaust valves (red curve) open at the end of the expansion stroke and remain open until the beginning of the intake stroke. The upper section of Figure 5 shows the pressure variation diagram on the piston head (in bar) as a function of the crankshaft rotational angle. Using these data and the piston head area, the gas force was calculated and converted to a time-based format, as shown in Figure 6.

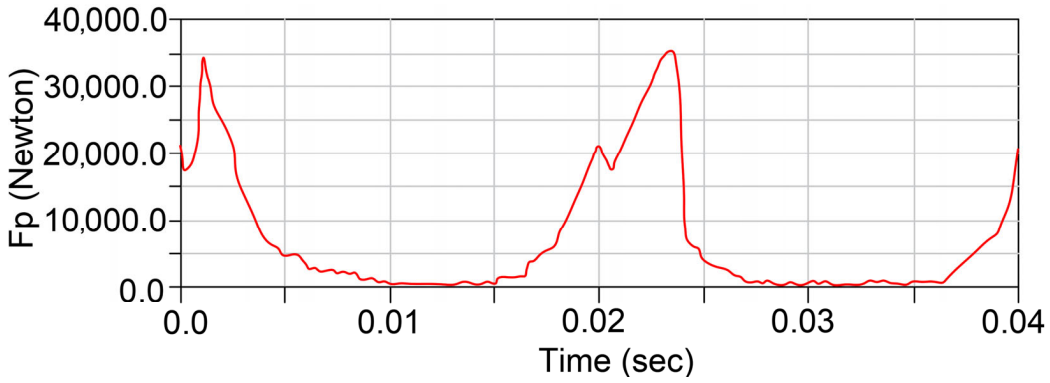


Figure 6. The force variation developed by the gas on the piston head.

The analysis will determine the positions, speeds, and accelerations of characteristic points *A* and *B*, along with the angular velocity and angular acceleration of the *AB* connecting rod, as shown in Figure 7.

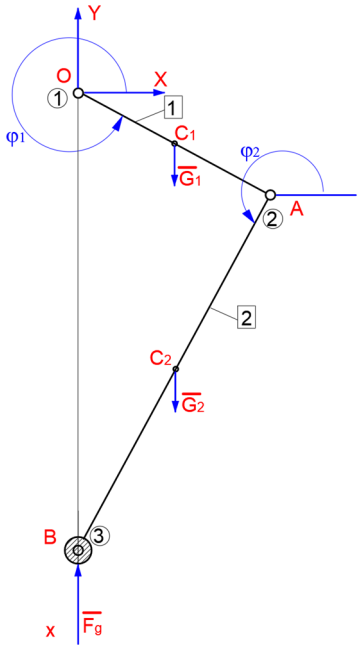


Figure 7. Finite elements and nodes.

The mechanism was then modeled using beam elements (see Figures 7 and 8).

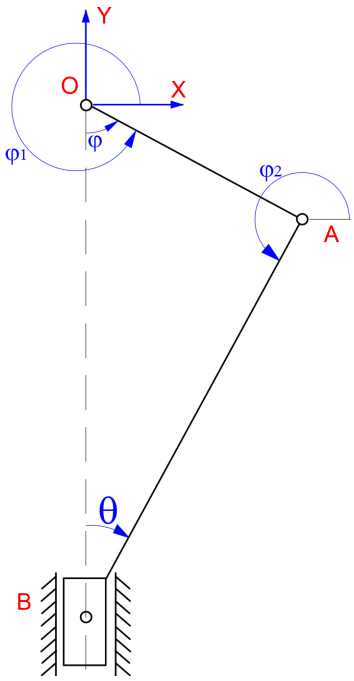


Figure 8. Mechanism kinematic scheme.

Each kinematic link of the mechanism is modeled as two beam-type finite elements, each comprising two nodes at their ends, with each node having 3DoF (see Figures 9 and 10). The analysis considers both the self-weights of the finite elements and the force generated by gas pressure on the piston head (F_b) as applied loads. For finite element no. 2, the piston component can be represented by a concentrated mass, m_c.

The mechanical system's motion can be reported using the following reference systems:

- $R1(x1,y1,z1)$—mobile reference system attached to finite element no. 1;
- $R2(x2,y2,z2)$—mobile reference system attached to finite element no. 2;
- $R0(X0,Y0,Z0)$—global reference system.

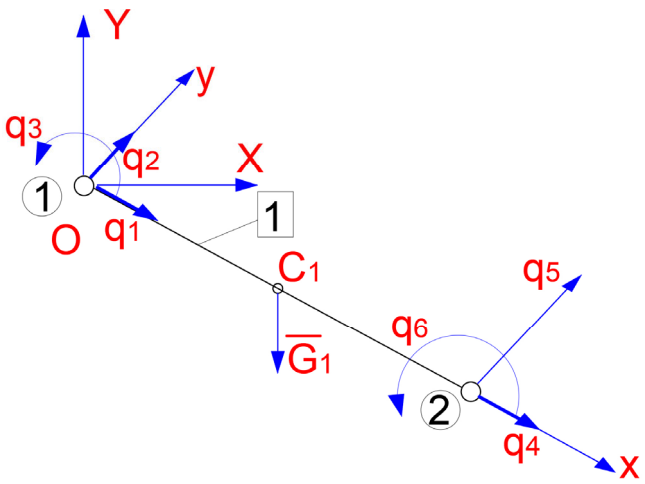


Figure 9. Finite element no. 1.

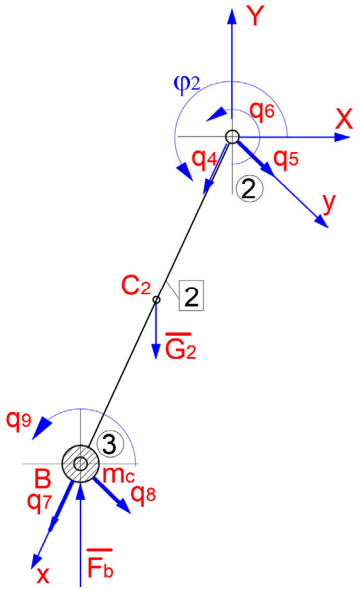


Figure 10. Finite element no. 2.

The proper mathematical model for the "e" finite element displacements is the following:

$$\left\{\vec{U^{(e)}}\right\} = \begin{Bmatrix} u(x) \\ v(x) \end{Bmatrix} = \left[N^{(e)}\right]\left\{\vec{q}^{(e)}\right\} \tag{43}$$

where $u(x)$—axial displacements; $v(x)$, $\theta(x)$—transversal displacements and angular displacements. From Equation (43) [20], we can identify the following:

$$\left[N^{(e)}\right] = \begin{bmatrix} 1-\frac{x}{l_e} & 0 & 0 & \frac{x}{l_e} & 0 & 0 \\ 0 & \frac{2x^3-3l_e x^2+l_e^3}{l_e^3} & \frac{x^3-2l_e x^2+l_e^2 x}{l_e^2} & 0 & -\frac{2x^3-3l_e x^2}{l_e^3} & \frac{x^3-l_e x^2}{l_e^2} \end{bmatrix} \tag{44}$$

$\left[N^{(e)}\right]$—the interpolation functions matrix (e = 1, 2);

$$\left\{\vec{q}^{(e)}\right\} = \begin{bmatrix} q_1 & q_2 & q_3 & q_4 & q_5 & q_6 \end{bmatrix}^T \tag{45}$$

$\left\{\vec{q}^{(e)}\right\}$—the nodal displacement vector for a finite element "e" with e = 1, 2 finite elements. This vector structure includes axial nodal displacements (q_1, q_4), transversal nodal displacements (q_2, q_5), and angular nodal displacements (q_3, q_6).

For the mechanism's assembled structure, we have the following:

$$\left\{\vec{q}\right\} = \begin{bmatrix} q_1 & q_2 & q_3 & q_4 & q_5 & q_6 & q_7 & q_8 & q_9 \end{bmatrix}^T \tag{46}$$

$\left\{\vec{q}\right\}$—nodal displacement vector in the local coordinate system.

The motion equations, in a matrix form for the mechanism, are as follows:

$$[M]\left\{\ddot{u}\right\} + [C]\left\{\dot{u}\right\} + [K]\{u\} = \{F\}, \tag{47}$$

where $[M]$—mass matrix, assembled for the entire analyzed mechanical system; $[K]$—assembled stiffness matrix; $[C]$—assembled damping matrix; $[F]$—nodal force vector, assembled for the entire mechanical system.

For the given mechanical system of two beam-type finite elements with 3 DoF per node, the motion equation matrices will be determined.

3.1. Nodal Force Calculus

The nodal forces corresponding to the local coordinates are determined using Equation (45). The nodal force static component, which corresponds to the finite element "*e*" (*e* = 1, 2), is as follows:

$$F_s^{(e)} = \rho^{(e)} g A^{(e)} \int_0^{l_1} [N_e]^T dx \tag{48}$$

where $\rho^{(e)}$—material density; g—gravitational acceleration; $A^{(e)}$—transversal section of the finite element "e", with e = 1, 2.

Finite element no.1:

The nodal force static component, expressed by taking into account the local reference system, is as follows:

$$f_s^{(1)} = F_s^{(1)} \begin{bmatrix} \sin\varphi_1 \\ -\cos\varphi_1 \\ 0 \end{bmatrix} \tag{49}$$

The nodal force dynamic component is the following:

$$\left[F_d^{(1)}\right] = \rho^{(1)} A^{(1)} \int_0^{l1} \left\{ \{r_1\}^T \left[\tilde{\omega}_{01}\right] \cdot \left[\tilde{\omega}_{01}\right] [N_1] \right\} dx \tag{50}$$

The angular speed can be written as an antisymmetric matrix as follows (i = 1, 2):

$$\left[\tilde{\omega}_{0i}\right] = \begin{bmatrix} 0 & -\omega_{0i}^z & \omega_{0i}^y \\ \omega_{0i}^z & 0 & -\omega_{0i}^x \\ -\omega_{0i}^y & \omega_{0i}^x & 0 \end{bmatrix} \tag{51}$$

Finite element no. 2:

The nodal force static component, relative to the local reference system, is as follows:

$$\left[f_s^{(2)}\right] = \left[F_s{}^{(2)}\right] \begin{bmatrix} -\sin\varphi_2 \\ \cos\varphi_2 \\ 0 \end{bmatrix} + f_g \tag{52}$$

The force generated by gas pressure in the local reference system, acting at node no. 3, is described as follows:

$$f_g = \begin{bmatrix} 0 & 0 & 0 & -F_g \sin\varphi_2 & F_g \cos\varphi_2 & 0 \end{bmatrix}^T \tag{53}$$

The dynamic components are the following:

$$\left[F_d^{(2)}\right] = -\iiint_{V^{(l)}} \rho^{(2)} [N_2]^T \left\{ \begin{pmatrix} \left[\tilde{\varepsilon}_{02}\right] + \left[\tilde{\omega}_{02}\right] \cdot \left[\tilde{\omega}_{02}\right] \cdot \{r_2\} + \\ + [A_{12}] \cdot \begin{pmatrix} \left\{\ddot{p}_2\right\} + 2[\tilde{\omega}_{01}]\left\{\dot{p}_2\right\} + \\ + \left[\tilde{\varepsilon}_{01}\right] + \left[\tilde{\omega}_{01}\right] \cdot \left[\tilde{\omega}_{01}\right] \end{pmatrix} \{p_2\} \end{pmatrix} \right\} dv, \tag{54}$$

where

$\{r_2\}$—is the B point vector in the local coordinate system, $R_2(x_2,y_2,z_2)$:

$$\{r_2\} = \begin{bmatrix} l_2 & 0 & 0 \end{bmatrix}^T \tag{55}$$

$\{p_2\}$—is the generalized coordinate vector for finite element no. 2 (mass center position and finite element no. 2 orientation):

$$\{p_2\} = \begin{bmatrix} x_2 & y_2 & \varphi_2 \end{bmatrix}^T \tag{56}$$

$\left\{\dot{p}_2\right\} = \frac{dp_2}{dt}, \left\{\ddot{p}_2\right\} = \frac{d^2p_2}{dt^2}$ is the vector of generalized speeds and accelerations.

$\{\omega_i\} = \frac{d\varphi_i}{dt} = \dot{\varphi}_i$, $\{\varepsilon_i\} = \ddot{\varphi}_i$; $i = 1, 2$ are the angular speed and the angular acceleration of the kinematic element "i".

The coordinate transformation matrix for crossing from a local axis reference system $R_i(x_i,y_i,z_i)$ to a global reference system $R_0(X_0,Y_0,Z_0)$ is as follows:

$$[A_{0i}] = \begin{bmatrix} \cos(\varphi_i) & -\sin(\varphi_i) & 0 \\ \sin(\varphi_i) & \cos(\varphi_i) & 0 \\ 0 & 0 & 1 \end{bmatrix}; i = 1, 2 \tag{57}$$

In this case, the coordinate transformation matrix for crossing from a local axis reference system $R_1(x_1,y_1,z_1)$ to a global reference system $R_2(x_2,y_2,z_2)$ is as follows:

$$[A_{12}] = \begin{bmatrix} \cos(\varphi_1 - \varphi_2) & -\sin(\varphi_1 - \varphi_2) & 0 \\ \sin(\varphi_1 - \varphi_2) & \cos(\varphi_1 - \varphi_2) & 0 \\ 0 & 0 & 1 \end{bmatrix} \tag{58}$$

The force which actuates on the finite element "e", (e = 1, 2), in the local axis system, is the following:

$$[f_e] = \left[f_s^{(e)}\right] + \left[F_d^{(e)}\right] \tag{59}$$

The force which actuates on the finite element "e" in the global axis system is as follows:

$$[F_e] = [T_e]^T [f_e], e = (1, 2) \tag{60}$$

where $[T_e]$ is the coordinate transformation matrix for crossing from a reference system attached to finite element "e" to a global reference system.

The assembled nodal force for the engine mechanism, according to the global reference system, is as follows:

$$[F] = \begin{bmatrix} F_{11}^{(1)} & F_{21}^{(1)} & F_{31}^{(1)} & F_{41}^{(1)} + F_{11}^{(2)} & F_{51}^{(1)} + F_{21}^{(2)} & F_{61}^{(1)} + F_{31}^{(2)} & F_{41}^{(2)} & F_{51}^{(2)} & F_{61}^{(2)} \end{bmatrix}^T \tag{61}$$

3.2. Stiffness Matrix

Static component. The stiffness matrix in a local coordinate system for the finite element "e", (e = 1, 2) is as follows:

$$\left[K_s^{(l_e)}\right] = \iiint_{v^{(e)}} [B]^T [D][B] dv = E^{(e)} A^{(e)} \int_0^{l_e} [B]^T [B] dx, \tag{62}$$

where $[B] = \left[\frac{12x-6l_e}{{l_e}^3} \quad \frac{6x-4l_e}{{l_e}^2} \quad -\frac{12x-6l_e}{{l_e}^3} \quad \frac{6x-2l_e}{{l_e}^2}\right]$—for transversal displacements; $[D] = E$—material elasticity modulus; $[B] = \left[-\frac{1}{l_e} \quad \frac{1}{l_e}\right]$—for axial displacements.

The stiffness matrix for finite element no. 1 is obtained by assembling the stiffness matrices corresponding to the transverse and axial displacements.

Dynamic component: For finite element no. 1, in the local axis reference system, the following can be obtained:

$$\left[K_d^{(l_1)}\right] = \iiint\limits_{v^{(e)}} \rho^{(1)}[N_1]^T \left(\begin{bmatrix} \overset{\bullet}{\widetilde{\omega}}_{01} \end{bmatrix} + \left[\widetilde{\omega}_{01}\right]\left[\widetilde{\omega}_{01}\right] \right)[N_1]dv \tag{63}$$

The stiffness matrix for finite element no. 2 is obtained by assembling the stiffness matrices corresponding to the transverse and axial displacements.

The dynamic component of the stiffness matrix in a local axis reference system, for finite element no. 2, is as follows:

$$\left[K_d^{(l2)}\right] = \rho^{(2)}A^{(2)} \int\limits_0^{l_2} [N_2]^T \begin{bmatrix} -{\omega_2}^2 & -\varepsilon_2 & 0 \\ \varepsilon_2 & -{\omega_2}^2 & 0 \\ 0 & 0 & 0 \end{bmatrix} [N_2]dx \tag{64}$$

The stiffness matrix for the finite element "*e*" (*e* = 1,2), according to the local reference system, is as follows:

$$\left[K^{(l_e)}\right] = \left[K_s^{(l_e)}\right] + \left[K_d^{(l_e)}\right] \tag{65}$$

The stiffness matrix for the finite element "e" (*e* = 1,2), according to the global reference system, is as follows:

$$\left[K^{(e)}\right] = [T_e]^T \left[K^{(l_e)}\right][T_e] \tag{66}$$

3.3. Mass Matrix

Finite element no. 1:

$$M^{(l_1)} = \iiint\limits_{V^{(e)}} \rho^{(1)}[N_1]^T[N_1]dv = \rho^{(e)}A^{(e)} \int_0^l [N_1]^T [N_1]dx \tag{67}$$

Finite element no. 2:

$$M^{(l_2)} = \iiint\limits_{V^{(2)}} \rho^{(2)}[N_2]^T[N_2]dv = \rho^{(2)}A^{(2)} \int_0^{l_2} [N_2]^T [N_2]dx + \left[m_p\right], \tag{68}$$

where "m_p" is the piston mass; $\rho^{(1,2)}$—finite element mass; [$N_{1,2}$]—form function matrix (interpolating ones).

The piston was considered a concentrated mass, which was attached to finite element no. 2 in node no. 3.

The mass matrix in a global coordinate system is the following:

Finite element "*e*" (*e* = 1, 2):

$$\left[M^{(e)}\right] = [T_e]^T \left[M^{(l_e)}\right][T_e] \tag{69}$$

The assembled equilibrium equations, in a global coordinate system, have the following form:

$$\begin{matrix} [K][Q] = [F] \\ [Q] = [K]^T[F] \end{matrix}, \tag{70}$$

where [*K*] is the assembled stiffness matrix; [*Q*] is the assembled nodal displacement vector; [*F*] represents the assembled nodal force vector.

3.4. The Assembly of the Equations and Introducing the Contour Conditions

Contour conditions will be introduced as follows: node no. 1 has a single DoF, which allows for only the Q_3 rotation, and node no. 3 has two DoFs, with the Q_8 displacement canceled for this configuration:

Finite element no. 1: $x = 0 \rightarrow Q_1 = 0; Q_2 = 0$;

Finite element no. 2: $x = l_2 \rightarrow Q_8 = 0$.

By considering the contour conditions, from the assembled matrix, which interact in the motion equation, [*M*], [*K*], and [*C*] and line 1, column 1; line 2, column 2; and line 8, column 8 will be canceled, respectively. Under these circumstances, the remaining matrices will have 6×6 dimensions.

The reduced mass matrix has the following form:

$$[M_r]\begin{bmatrix} M_{33}^{(1)} & M_{34}^{(1)} & M_{35}^{(1)} & M_{36}^{(1)} & 0 & 0 \\ M_{43}^{(1)} & M_{44}^{(1)}+M_{11}^{(2)} & M_{45}^{(1)}+M_{12}^{(2)} & M_{46}^{(1)}+M_{13}^{(2)} & M_{14}^{(2)} & M_{16}^{(2)} \\ M_{53}^{(1)} & M_{54}^{(1)}+M_{21}^{(2)} & M_{55}^{(1)}+M_{22}^{(2)} & M_{56}^{(1)}+M_{23}^{(2)} & M_{24}^{(2)} & M_{26}^{(2)} \\ M_{63}^{(1)} & M_{64}^{(1)}+M_{31}^{(2)} & M_{65}^{(1)}+M_{32}^{(2)} & M_{66}^{(1)}+M_{33}^{(2)} & M_{34}^{(2)} & M_{36}^{(2)} \\ 0 & M_{41}^{(2)} & M_{42}^{(2)} & M_{43}^{(2)} & M_{44}^{(2)} & M_{46}^{(2)} \\ 0 & M_{61}^{(2)} & M_{62}^{(2)} & M_{63}^{(2)} & M_{64}^{(2)} & M_{66}^{(2)} \end{bmatrix} \tag{71}$$

The reduced stiffness matrix has the following form:

$$[K_r]\begin{bmatrix} K_{33}^{(1)} & K_{34}^{(1)} & K_{35}^{(1)} & K_{36}^{(1)} & 0 & 0 \\ K_{43}^{(1)} & K_{44}^{(1)}+K_{11}^{(2)} & K_{45}^{(1)}+K_{12}^{(2)} & K_{46}^{(1)}+K_{13}^{(2)} & K_{14}^{(2)} & K_{16}^{(2)} \\ K_{53}^{(1)} & K_{54}^{(1)}+K_{21}^{(2)} & K_{55}^{(1)}+K_{22}^{(2)} & K_{56}^{(1)}+K_{23}^{(2)} & K_{24}^{(2)} & K_{26}^{(2)} \\ K_{63}^{(1)} & K_{64}^{(1)}+K_{31}^{(2)} & K_{65}^{(1)}+K_{32}^{(2)} & K_{66}^{(1)}+K_{33}^{(2)} & K_{34}^{(2)} & K_{36}^{(2)} \\ 0 & K_{41}^{(2)} & K_{42}^{(2)} & K_{43}^{(2)} & K_{44}^{(2)} & K_{46}^{(2)} \\ 0 & K_{61}^{(2)} & K_{62}^{(2)} & K_{63}^{(2)} & K_{64}^{(2)} & K_{66}^{(2)} \end{bmatrix} \tag{72}$$

The nodal force for the engine mechanism, relative to the global reference system, is as follows:

$$[F_r] = \begin{bmatrix} F_{31}^1 & F_{41}^1+F_{11}^2 & F_{51}^1+F_{21}^2 & F_{61}^1+F_{31}^2 & F_{41}^2 & F_{61}^2 \end{bmatrix}^T \tag{73}$$

The elastic displacement vector for element "*e*" (*e* = 1,2) is as follows:

$$\left[\vec{U^{(e)}}\right] = [N_e]\left[\vec{Q^{(e)}}\right] \tag{74}$$

$$\left[\vec{Q}\right] = \left[K_r^T\right]\left[\vec{F_r}\right] \tag{75}$$

The nodal displacement vector for finite element no. 1, in the global reference system, is as follows:

$$\left[\vec{Q^{(1)}}\right] = \begin{bmatrix} Q_1 & Q_2 & Q_3 & Q_4 & Q_5 & Q_6 \end{bmatrix}^T, \tag{76}$$

where $Q_1 = 0$; $Q_2 = 0$ (by introducing the contour conditions).

The nodal displacement vector for finite element no. 2, in the global reference system, has the following form:

$$\left[\vec{Q^{(2)}}\right] = \begin{bmatrix} Q_4 & Q_5 & Q_6 & Q_7 & Q_8 & Q_9 \end{bmatrix}^T \tag{77}$$

where $Q_8 = 0$ (by introducing the contour conditions).

3.5. Modal Dynamic Analysis

The motion equations, without damping, are as follows:

$$[M]\left\{\ddot{q}\right\} + [K]\{q\} = \{F\} \tag{78}$$

The differential equation without damping and external loads is as follows:

$$[M]\left\{\ddot{q}\right\} + [K]\{q\} = 0 \tag{79}$$

The modal superposition method will be used to solve the motion equation system (78). This approach simplifies the equations using a linear transformation:

$$q_i(t) = \sum_{j=1}^{n} \phi_{ij} a_j(t), i = \overline{1,n}, \tag{80}$$

where ϕ_{ij} is the modal form coordinate which represents the "i" mass position in a "j" mode; $a_j(t)$ is the generalized coordinate which represents the "j" mode response during time; ϕ_{ij} depends on the position, not on time; $a_j(t)$ depends on time and not on the position.

Under a matrix form, the following is obtained:

$$\{q\} = [\phi]\{a(t)\} \tag{81}$$

where $[\phi]$—modal matrix, where the modal forms will be written in columns.

It is acknowledged that the modal form vectors are orthogonal with respect to the mass matrix, which implies the following:

$$[\phi]^T[M][\phi] = I - \text{unit matrix} \tag{82}$$

The mathematical expression (81) is differentiated twice.

$$\left\{\ddot{q}\right\} = [\phi]\left\{\ddot{a}(t)\right\} \tag{83}$$

And by introducing (81) and (83) in (78), we obtain the following:

$$[M][\phi]\left\{\ddot{a}(t)\right\} + [K][\phi]\{a(t)\} = \{F(t)\} \tag{84}$$

We multiply the left side of the (84) relation by the $[\phi]^T$ term and take into account Equation (82); we then obtain the following:

$$\left\{\ddot{a}(t)\right\} + [\phi]^T[K][\phi]\{a(t)\} = [\phi]^T\{F(t)\} \tag{85}$$

From (79), we can obtain the following:

$$\omega^2[M][\phi] = [K][\phi] \tag{86}$$

In the mathematical expression (86), we multiply the left side by $\{\phi\}^T$, and taking into account (82), we obtain the following:

$$\left[\omega^2\right] = [\phi]^T[K][\phi] \tag{87}$$

We introduce (87) in (85) and obtain the following:

$$\{\ddot{a}(t)\} + \left[\omega^2\right]\{a(t)\} = [\phi]^T\{F(t)\} \tag{88}$$

The mathematical expression (88) describes an uncoupled set of independent differential equations. For the analyzed case, the modal frequencies are as follows:

$$\left[\omega^2\right] = diag\left[\omega_1^2, \omega_2^2, \ldots \omega_6^2\right] \tag{89}$$

We reconsider the following equation:

$$\left([K] - \omega^2[M]\right)\{\phi\} = 0 \tag{90}$$

where $\phi = \left[\phi_{ij}\right]; i, j = 1 \ldots 6$ is the modal matrix form.

The natural frequencies are as follows: $f_i = \omega_i/2\pi, i = 1 \ldots 6$, where $f_1 = 4.957487532$ Hertz; $f_2 = 542.9548523$ Hertz; $f_3 = 156.8132854$ Hertz; $f_4 = 3230.572390$ Hertz; $f_5 = 978.5360786$ Hertz; $f_6 = 93.29474415$ Hertz.

Based on numerical analysis, the diagrams presented in Figures 11–16 illustrate six distinct vibration modes identified for the mechanism under study.

In the mathematical model, for each flexible component of the system, six frequencies were selected, which corresponds to six modal forms. This selection was performed in a frequency domain of [0–1000] Hertz, and it corresponds to the angular speeds of the crankshaft and connecting rod. The modal analysis gives information about avoiding mechanical resonance phenomena.

The generalized coordinates, which are the result after solving the equation system (88), are as follows:

$$\{a(t)\} = \left[a_1(t) \quad a_2(t) \quad a_3(t) \quad a_4(t) \quad a_5(t) \quad a_6(t)\right]^T \tag{91}$$

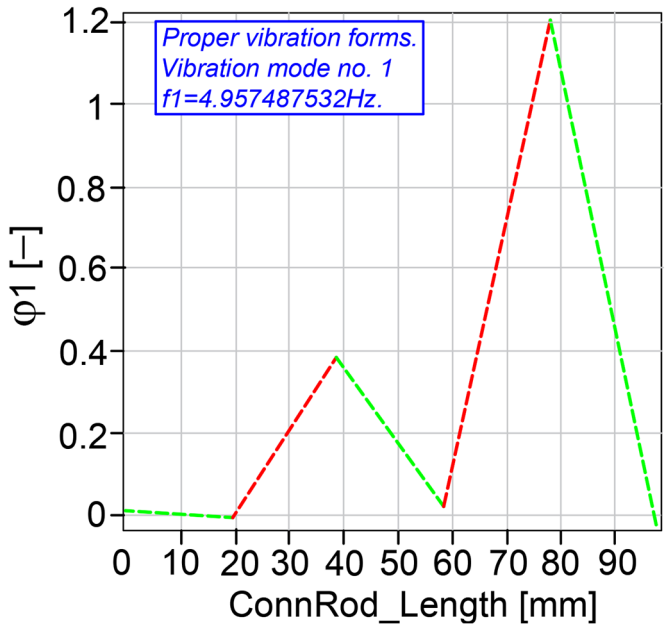


Figure 11. Vibration mode no. 1, at f1 frequency.

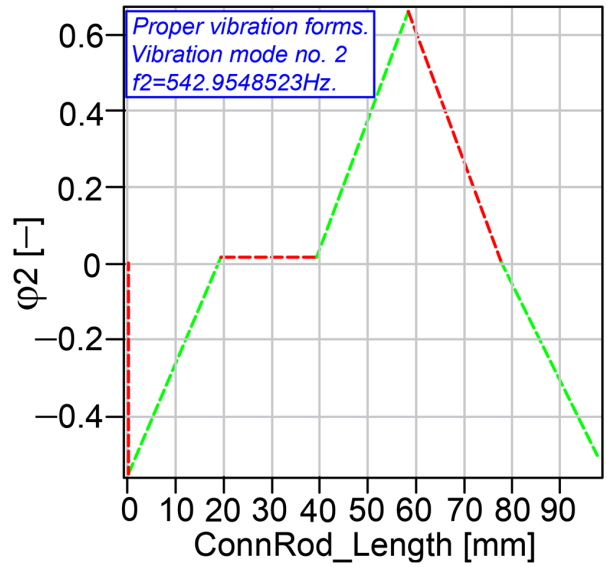


Figure 12. Vibration mode no. 2, at f2 frequency.

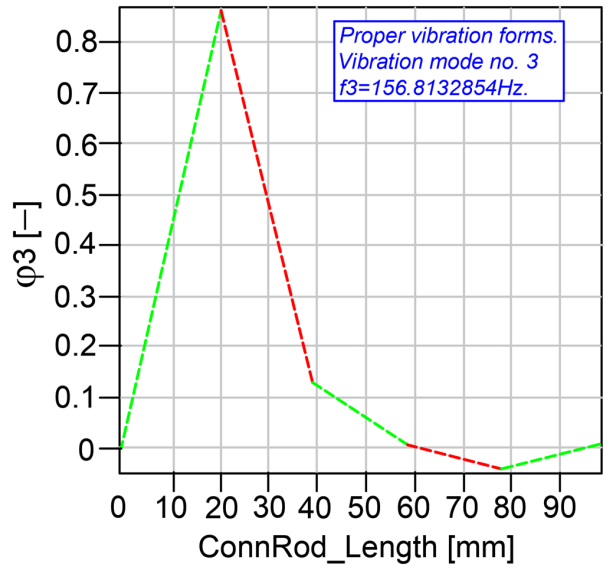


Figure 13. Vibration mode no. 3, at f3 frequency.

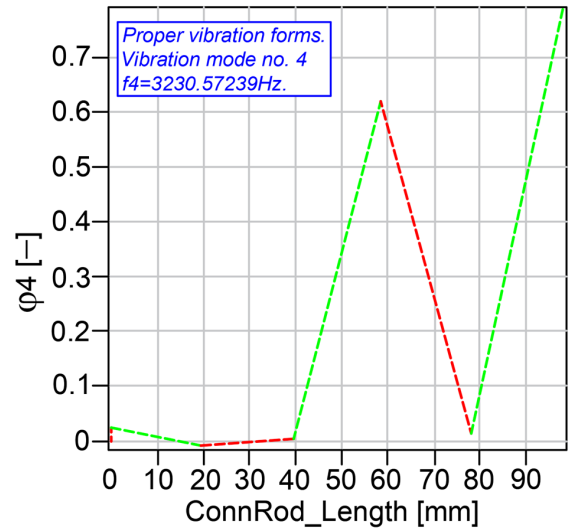


Figure 14. Vibration mode no. 4, at f4 frequency.

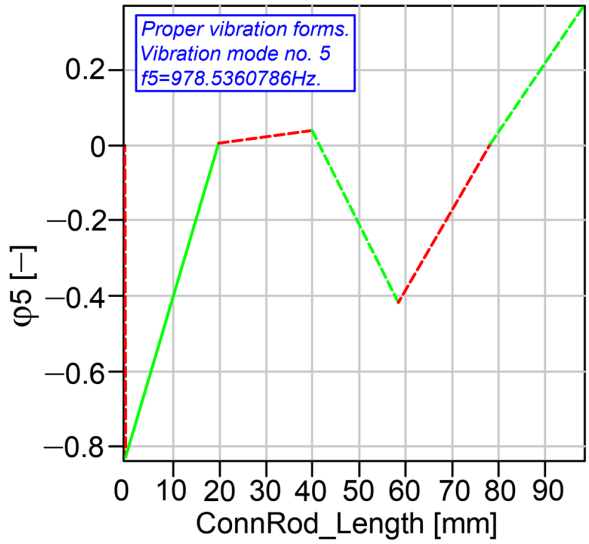


Figure 15. Vibration mode no. 5, at f5 frequency.

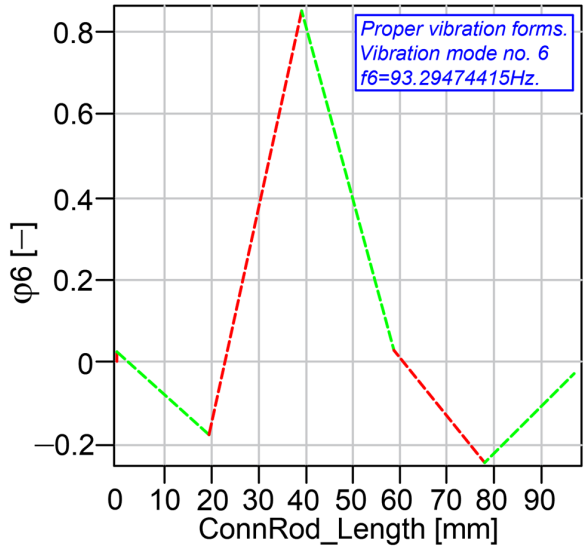


Figure 16. Vibration mode no. 6, at f6 frequency.

The solution to the equation system (78) is obtained by solving the differential equation system (88). By knowing the generalized coordinates from (91) and the modal matrix $\phi = [\phi_{ij}]$, $i,j = 1,\ldots, 6$, we obtain the nodal displacements $\{q\} = [\phi]\{a(t)\}$.

The elastic displacements can be obtained by solving the following equation system:

$$\{u\} = [N]\{q\} \tag{92}$$

3.6. Results of Numerical Processing

A program was created in the Maple programming environment for the numerical processing of mathematical models. This program supports simultaneous inverse dynamic analysis when the mechanism elements are modeled as rigid bodies, as well as elasto-dynamic and modal dynamic analysis when the elements are considered deformable bodies.

A 3D model of the engine mechanism was constructed as part of the virtual prototyping process. An interface was developed to import this model into the MSC Adams virtual environment.

In the initial phase, a numerical simulation of the mechanism's kinematic model was performed. Input data included the crankshaft rotation speed (6000 rpm), geometric characteristics, mass properties of the mechanism's kinematic links, and the local reference systems associated with the specified links and kinematic joints. The motion of the mechanism was analyzed over a time interval of 0.04 s, during which the engine crankshaft completed four full rotations.

In the second stage, a dynamic model was developed. The gas pressure applied to the piston head and the geometry, material characteristics, and inertial properties of the kinematic links are specified.

The torque variation law acting on the crankshaft was determined and, consequently, the variation in the engine crankshaft angular speed.

The pressure exerted by the gas on the piston head was measured experimentally, and its variation as a function of the crankshaft rotation angle is presented in Figure 5.

In order to determine the crankshaft torque (engine torque), a function was created that enables the interface with the ADAMS programming environment, as follows:

$$M_m = M_0 \times (1 - WX(MARKER_I, MARKER_J, MARKER_J)/\omega_0) \quad (93)$$

where "Mm" is the engine torque; "M_0" is the initial torque; "ω_0" is the initial angular speed; $WX(MARKER_I, MARKER_J)$ is the X-axis component corresponding to the crankshaft angular speed, between marker "I" and marker "J", measured in accordance with the coordinate system attached to marker "J".

For the analyzed case study, the torque function is given by the following:

$$M_m = -170000 \times (1 - WX(MARKER_1,MARKER_2,MARKER_2)/100) \quad (94)$$

Figure 17 illustrates snapshots from the virtual simulation carried out using MSC Adams 2017 software.

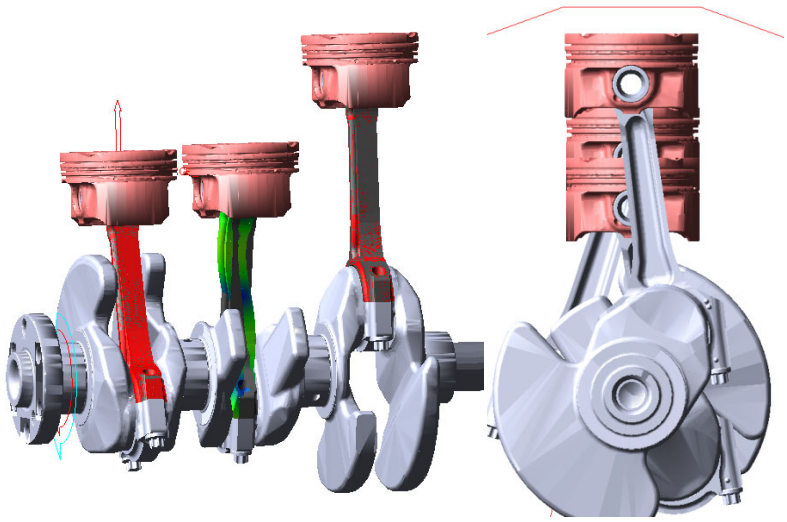


Figure 17. Dynamic model from Adams (connecting rod 2—mode 10; frequency 6425.318392722 Hertz).

The three connecting rods were analyzed as deformable bodies, with the transformation from rigid to deformable bodies being in accordance with the finite element method. To mesh the proposed model, a tetrahedral finite element was used.

The connecting rod linear and angular deformations were determined in the Adams programming environment, based on the theory developed by Craig & Bampton [22]. The results were compared with those from the processing of the mathematical models in the modal dynamic analysis, as shown in Figures 18–22.

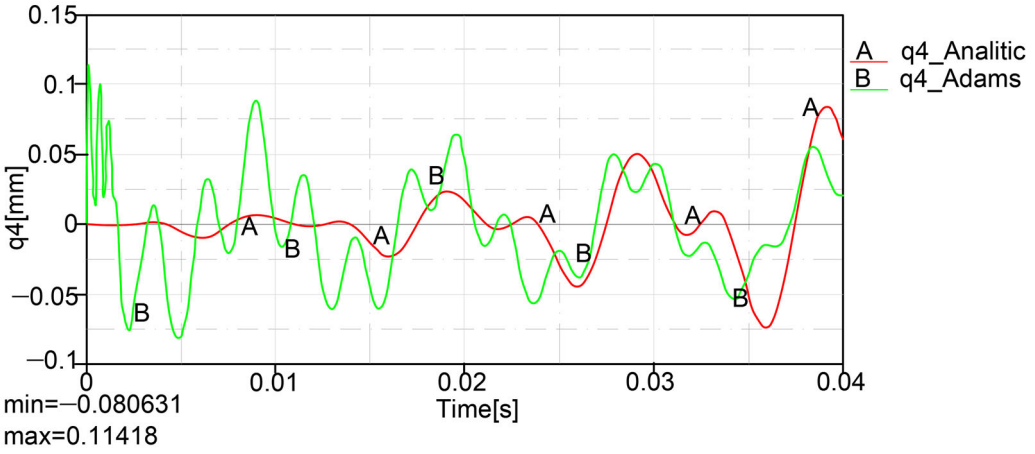


Figure 18. Axial nodal displacement variation on x-axis (q4).

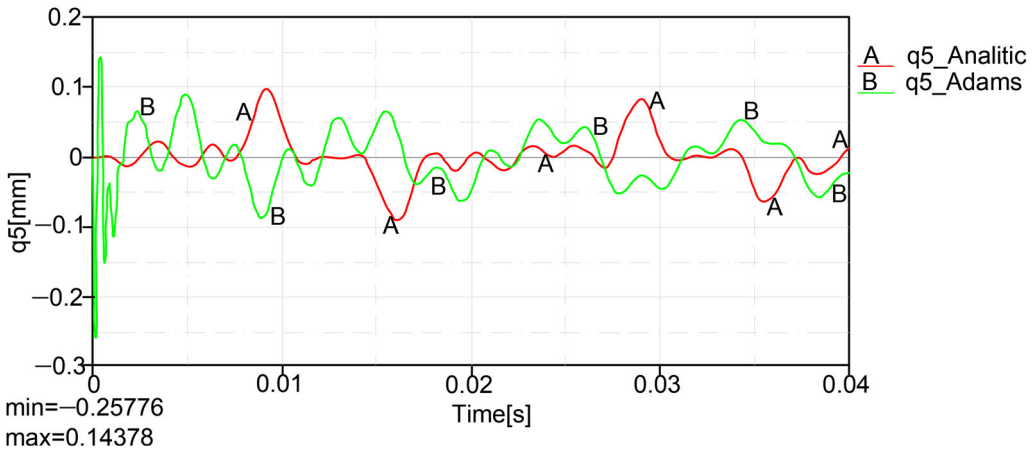


Figure 19. Transversal nodal displacement variation on y-axis (q5).

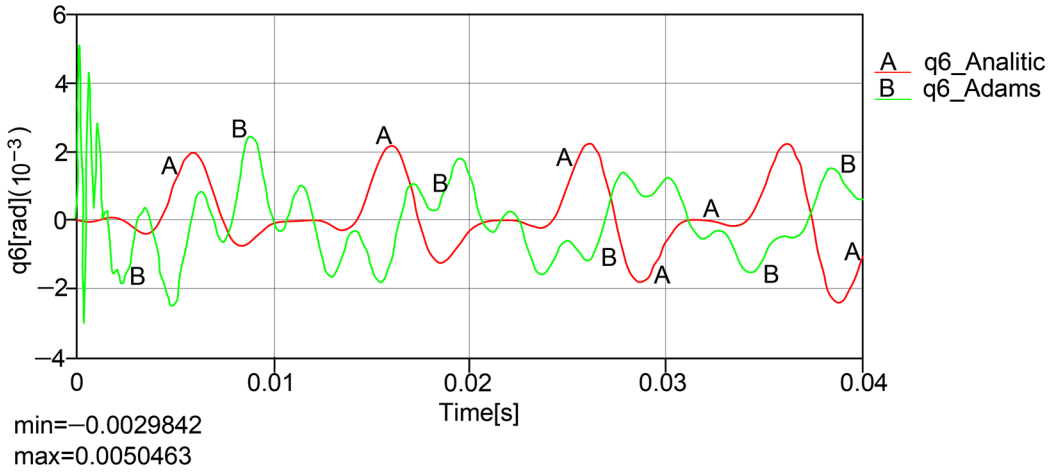


Figure 20. Angular nodal displacement variation (q6).

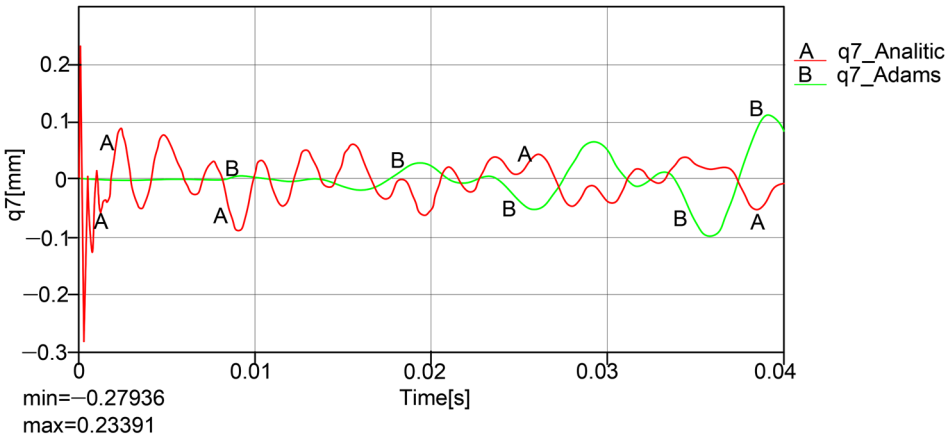


Figure 21. Linear nodal displacement variation on x-axis (q7).

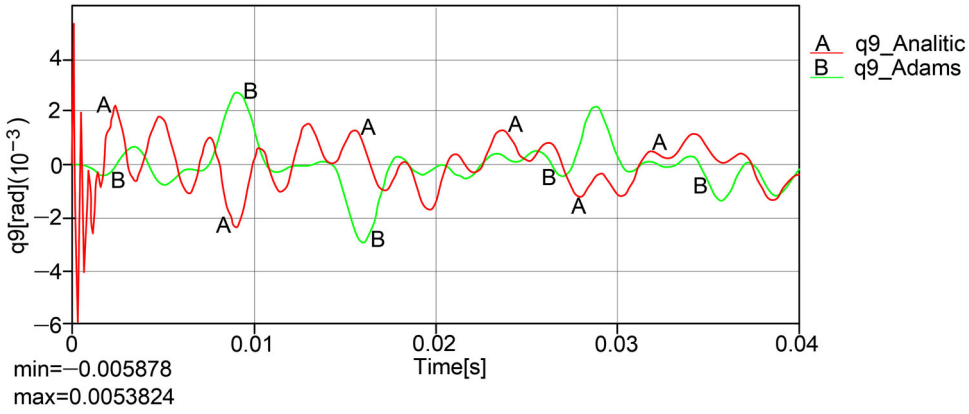


Figure 22. Angular nodal displacement variation (q9).

Considering the diagrams shown in Figures 18–22, it could be remarked that during the numerical processing under the MSC Adams environment, some spikes in the longitudinal, transversal, or angular nodal displacements were recorded at the beginning of motion in a short period of time (10^{-4} s). After this, the motion is stabilized. The recorded differences at the maximum values of the nodal displacements on some time intervals can be explained by the fact that the desired virtual prototyping dynamics were achieved on the proposed mechanism composed of a crankshaft, three deformable connecting rods, and three pistons. Thus, in Figure 18, it is shown that the axial nodal displacement records a maximum amplitude of 0.114 mm and a minimum one equal to −0.008 mm on the x-axis, which corresponds to "q_4". In the case of transversal displacement q_5, a maximum amplitude of 0.14378 mm and a minimum one of −0.257 mm were recorded on the y-axis, as can be seen in Figure 19. If we refer to angular nodal displacement, namely "q_6", a maximum amplitude of 0.005 radians and a minimum one equal to –0.02 radians were recorded, as reported in Figure 20. If we conduct a close comparative analysis between the values of the reported curves A (Analytic) and B (Adams) on time intervals, we find that close values were recorded, as can be seen in Table 1.

Table 1. Nodal angular displacements of q_6. Comparative study.

Time Interval	0–0.01 [s]	0.01–0.02 [s]	0.02–0.03 [s]	0.03–0.04 [s]
q6_Adams	0.0023	0.0017	0.0013	0.0014
q6_Analytic	0.0019	0.002	0.0017	0.002

If we refer to the linear displacement in the case of q_7 reported in the graph in Figure 21, we remark that the recorded maximum amplitude was 0.23391 millimeters, and a minimum value of -0.27 mm was obtained on the x-axis, which corresponds to the starting point of the virtual simulations. By referring to time intervals, a comparative analysis was conducted, and this is represented in Table 2, from which it can be remarked that close values and, in this way, both analyzed cases (analytical model and Adams model) can be validated.

Table 2. Nodal linear displacements of q_7. Comparative study.

Time Interval	0–0.01 [s]	0.01–0.02 [s]	0.02–0.03 [s]	0.03–0.04 [s]
q7_Adams	0.0096	0.058	0.032	0.04
q7_Analytic	0.011	0.087	0.038	0.039

By considering the angular nodal displacement q_9 presented in the graph in Figure 22, we observe that the amplitude maximum value was equal to 0.005 radians, and the minimum one was equal to -0.005 radians. In a similar mode, we can conduct a comparative study represented in Table 3 in order to validate both analyzed models, and it can be observed that in specific time intervals, the values are close to each other.

Table 3. Nodal angular displacements of q_9. Comparative study.

Time Interval	0–0.01 [s]	0.01–0.02 [s]	0.02–0.03 [s]	0.03–0.04 [s]
q9_Adams	0.00184	0.00086	0.0003	0.001
q9_Analytic	0.0019	0.001	0.00024	0.0012

By processing the relation (92), we obtained the time variation diagrams for the transverse and longitudinal displacements of the connecting rod, as indicated in Figures 23–28.

In Figures 25 and 26, the longitudinal and transversal displacement variations are shown, and these correspond to half of the connecting rod length. These were also the result of the numerical processing of mathematical models.

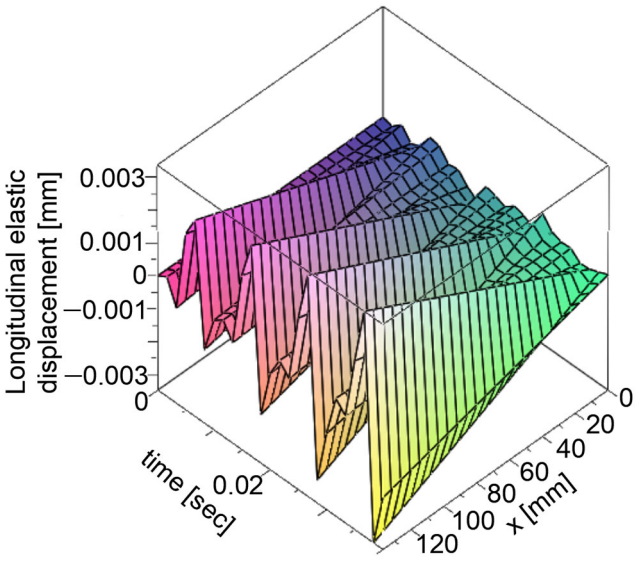


Figure 23. Longitudinal elastic displacement for element no. 2 in the global coordinate system.

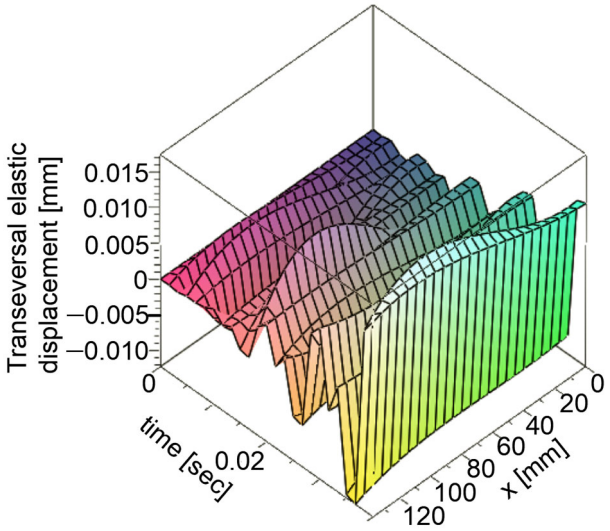


Figure 24. Transversal elastic displacement for element no. 2 in the global coordinate system.

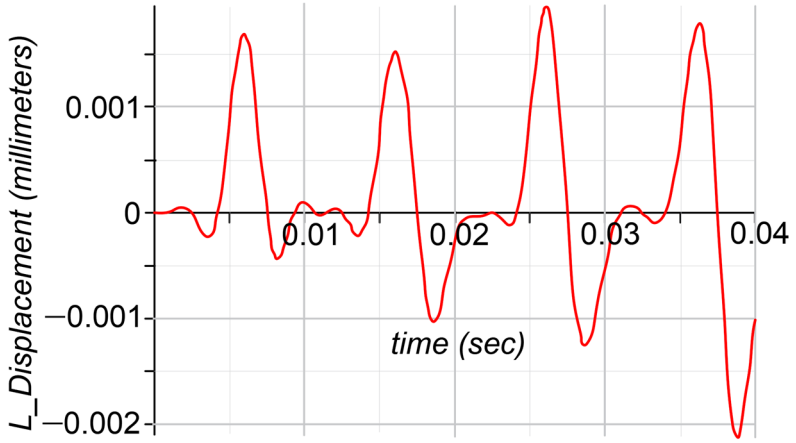


Figure 25. Longitudinal displacement variation at half the length of the connecting rod length.

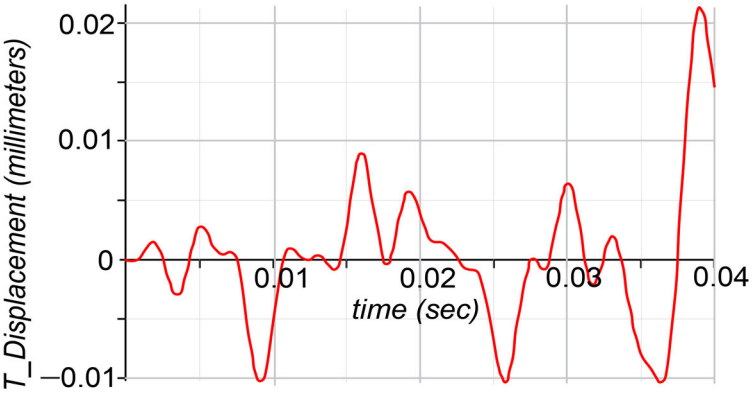


Figure 26. Transversal displacement variation at half the length of the connecting rod length.

The maximum value of longitudinal displacements is 0.003 mm, as can be observed in Figure 27. The recorded differences between the maximum values on time periods for the analytical model and the virtual one are almost negligible (10^{-3} mm).

The maximum value of transversal displacements is equal to 0.0214 mm. The measurements were performed at ½ the length of the connecting rod length. Thus, small differences between the maximum values of the elastic displacements were recorded, mainly between the mathematical model and the virtual one. It can be remarked that both the longitudinal

and transversal elastic displacements are at an order of 10^{-3} mm and 10^{-2} mm order, respectively, and these are acceptable values in design practice.

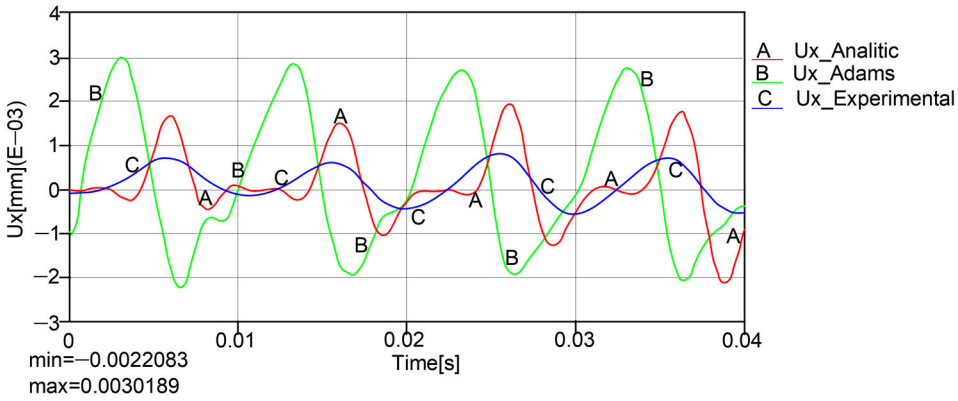


Figure 27. Comparative analysis of longitudinal elastic displacements.

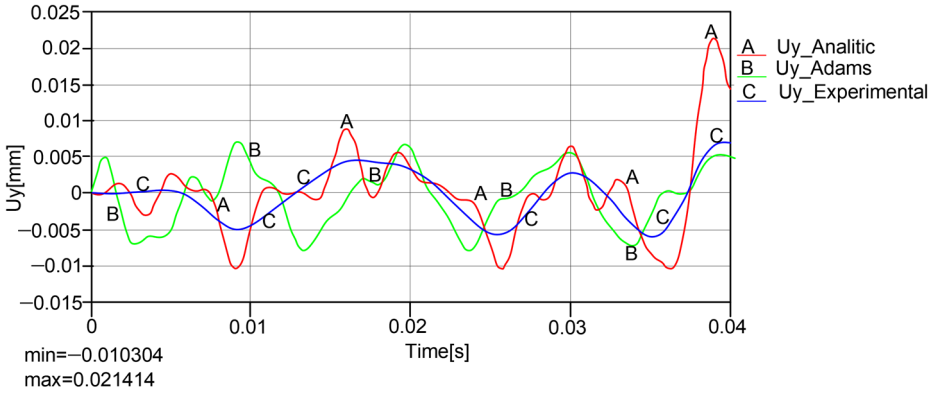


Figure 28. Comparative analysis of transversal elastic displacements.

The mathematical and virtual models allow us to obtain proper diagrams for the speeds and accelerations in the motion of the connecting rod considered a deformable body.

4. Experimental Analysis

An HBK WA—L-type inductive displacement transducer was employed to measure the piston stroke, installed through an aperture created in the engine cylinder head. The transducer is directly connected to the piston, allowing for the accurate monitoring of its stroke during the mechanism's operation, as can be seen in Figure 29.

We used an HBK WA—L inductive displacement transducer, installed via a dedicated hole in the cylinder head, to measure piston stroke. The sensor's mobile component attaches to the piston, enabling the precise measurement of piston movement during engine operation.

The characteristics of the transducer are the following:

- Transducer type: conductive, linear.
- High precision: compatible with dynamic measurements.
- Variable measuring domain: selected for covering the entire piston stroke.
- Rigid coupling: ensures measurement without mechanical interference.

This transducer is used to analyze the piston kinematics, providing experimental data for validating the theoretical models and the virtual simulations performed in MSC ADAMS.

A precision transducer enables comparison between the experimental results and predictions from numerical modeling, supporting data validation and allowing for the identification of any deviations from the impact theory used in the simulations.

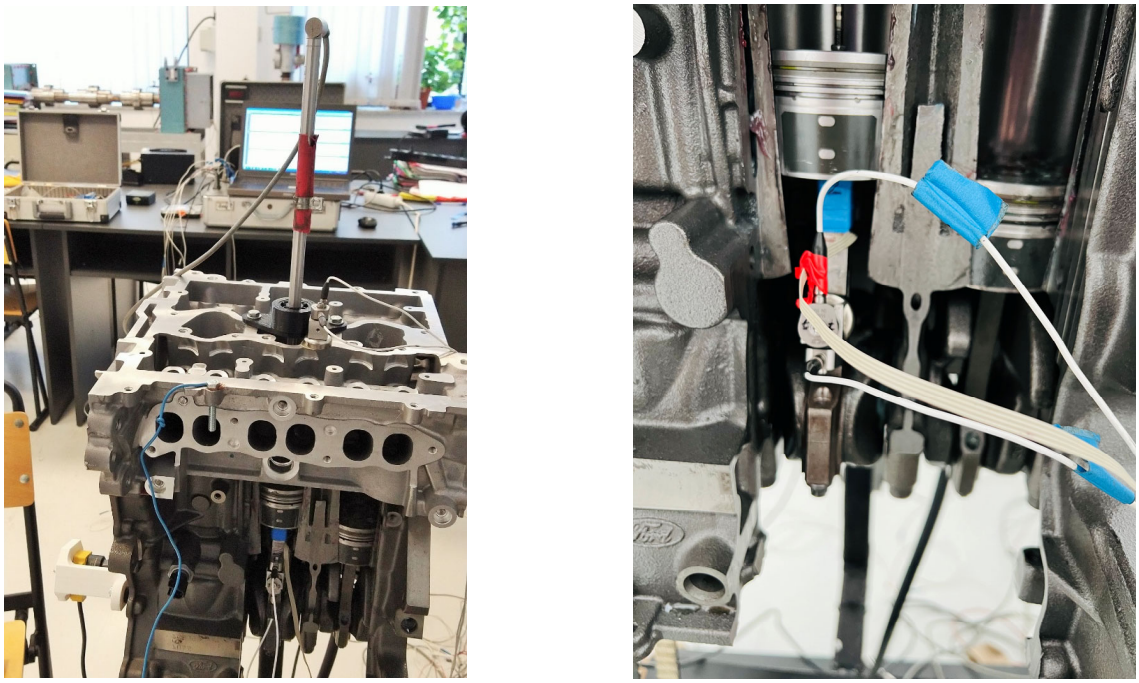


Figure 29. Experimental test rig for dynamic analysis of engine mechanism: detailed view for dynamic experimental analysis of piston–connecting rod mechanism.

For the dynamic analysis of the mechanism, piezoelectric acceleration transducers were employed. These sensors were installed on both the connecting rod and the cylinder head to measure longitudinal and transverse accelerations.

The configuration of the experimental setup is as follows:

- Connecting rod accelerometers were attached with magnets to the flat surface of the connecting rod, near the strain gauge areas, to ensure the accurate measurement of longitudinal and transversal acceleration.
- Cylinder head accelerometers were mounted above the analyzed piston, capturing the vibrations and accelerations transmitted through the engine.

The accelerometer's characteristics are as follows:

- Type: piezoelectric.
- Measurement range: ± 50 g.
- Sensitivity: 10 mVolts/grams.
- Mounting method: magnets for the connecting rod, screws for the cylinder head.
- Frequency domain: 0.5 Hertz–10 kHertz.

The accelerometers were used for the following reasons:

- To determine the vibrations induced during the motion of the connecting rod and piston.
- To compare the accelerations simulated in MSC.ADAMS with those experimentally measured.
- To validate the dynamic model through a frequency spectrum analysis of the measured accelerations.

Utilizing these accelerometers enabled the collection of critical data regarding the dynamic behavior of the system, thereby facilitating precise correlation between the simulation results and experimental measurements. The recorded parameters are as follows:

- AccBiela_L(meter/second^2)—connecting rod longitudinal acceleration;
- AccBiela_T(meter/second^2)—connecting rod transversal acceleration;
- AccBloc_V(meter/second^2)—cylinder head vertical acceleration;
- AccBloc_T(meter/second^2)—cylinder head transversal acceleration;
- CursaPiston(millimeters)—piston stroke;
- FortaBiele(Newton)—connecting rod longitudinal force.

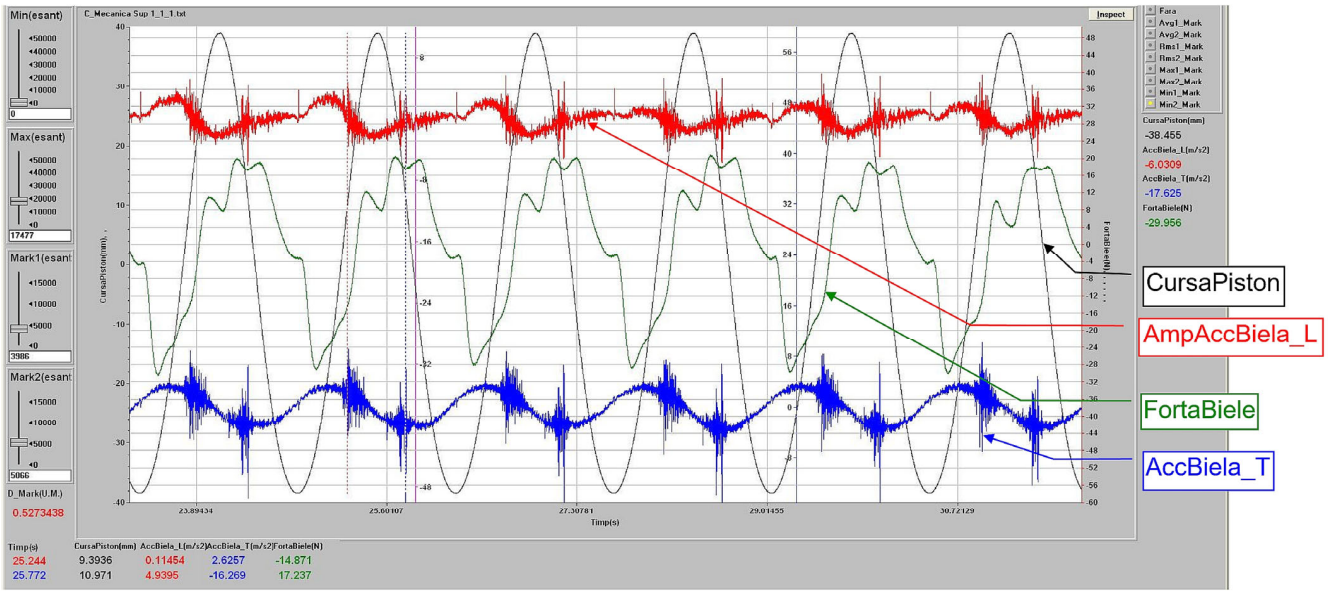
For a single connecting rod setup, experimental tests were carried out successively at three different excitation frequencies, as can be seen in Figure 29. The electric motor's operating frequency was adjusted using a frequency converter, with values around the following: 0.7 Hertz, 1 Hertz, and 1.3 Hertz.

For each excitation frequency, the operating time was approximately 30 s, allowing for a frequency analysis over a reasonably wide bandwidth. It is important to note that the frequency resolution is inversely proportional to the analysis signal length:

$$Df = 1/Dt \tag{95}$$

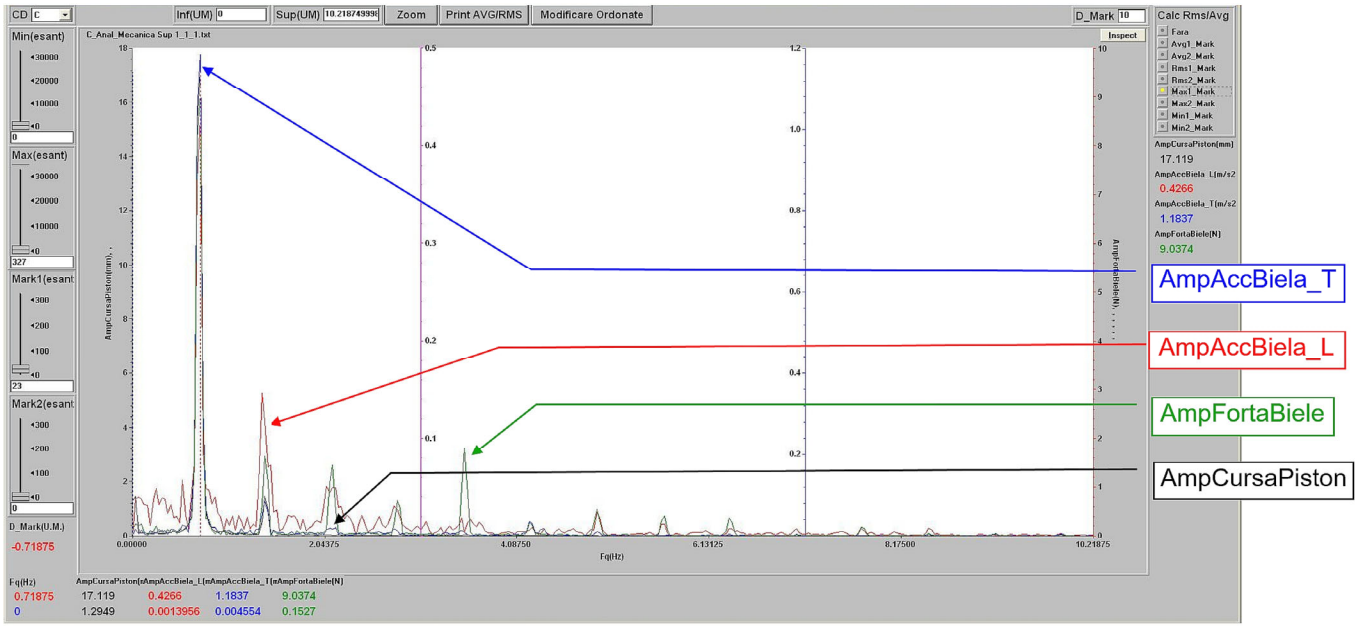
Considering the relation (95), in the frequency analyses performed, the frequency displayed on the screen represents the center of the frequency band, while the actual frequency lies within that band. For this reason, it was preferred that the excitation frequency of the piston be calculated from the time domain representations as the inverse of the piston stroke period. The experimental recordings were carried out using the LAN—XI data acquisition system, model 3053—B120, manufactured by Brüel & Kjær Darmstadt Germany, along with the Pulse Labshop 8.0 software from the same manufacturer.

Post-processing analyses were performed using the Pulse Reflex and TestPoint 8700 software packages, which complement each other, and the results of these are shown in Figures 30 and 31.



Parameter	CursaPiston (mm)	AccBiela_L (m/s²)	AccBiela_T (m/s²)	FortaBiele (N)
RMS	27.49938	1.287273	2.494962	15.64239
Max	38.93359	5.932628	9.160046	20.45467
Min	−38.4553	−6.03089	−17.6255	−29.9561

Figure 30. Time analysis for recordings on the connecting rod at a frequency of 0.706 Hertz.



Frequency (Hz)	CursaPiston (mm)	AccBiela_L (m/s²)	AccBiela_T (m/s²)	FortaBiele (N)
0.71875	17.11938	0.426604	1.18365	9.037379
1.375	1.451152	0.145541	0.084355	1.621429
2.125	0.037748	0.050018	0.021087	1.436896
2.812499999	0.041518	0.030532	0.017492	0.719175
3.531249999	0.037987	0.018159	0.011946	1.777926

Figure 31. Frequency analysis for recordings on the connecting rod at a frequency of 0.706 Hertz.

For the connecting rod, as can be noticed in Figure 30, the accelerations predominantly exhibit a sinusoidal pattern, with two impact zones occurring on either side of the piston stroke's peak moment, corresponding to the points where the direction of the force acting through the connecting rod changes on the two lateral faces of the piston.

From the time domain analysis of the connecting rod vibrations, it is observed that the longitudinal and transversal accelerations predominantly exhibit a sinusoidal pattern, with two impact zones on either side of the maximum point of the piston stroke. These correspond to the moments when the direction of the force transmitted by the connecting rod changes to the two lateral faces of the piston; see Figure 31.

The longitudinal force in the connecting rod shows inflection points at the maximum and minimum points of the piston stroke. These inflection points should be delimited in the case of a connecting rod without clearances in the joints.

Thus, by considering the acquired experimental accelerations, which mainly correspond to the accelerometer mounted on the connecting rod body, from Figure 29, a comparative analysis was conducted, by taking into account the results from the analytical model and virtual prototyping presented in the previous sections of this research. The comparative analysis can be summarized by the plots in Figures 32 and 33.

Thus, in Figure 32, the longitudinal accelerations obtained through the three mentioned methods are represented, including the ones obtained through mathematical model processing, virtual prototyping, and experimental analysis. The recorded differences can be explained by the fact that between the experimental model and the other two models (virtual and mathematical models), the results are influenced by possible clearances which may occur inside of the joints, measurement accuracy, material properties, and so on. The

obtained extreme values are suitable for the limit interval, which is $-2.5,\ldots,1.8$ (m/s^2). Also, we remark that the obtained results in the case of the mathematical model are also suitable as a form variation and extreme values in the previous mentioned domain.

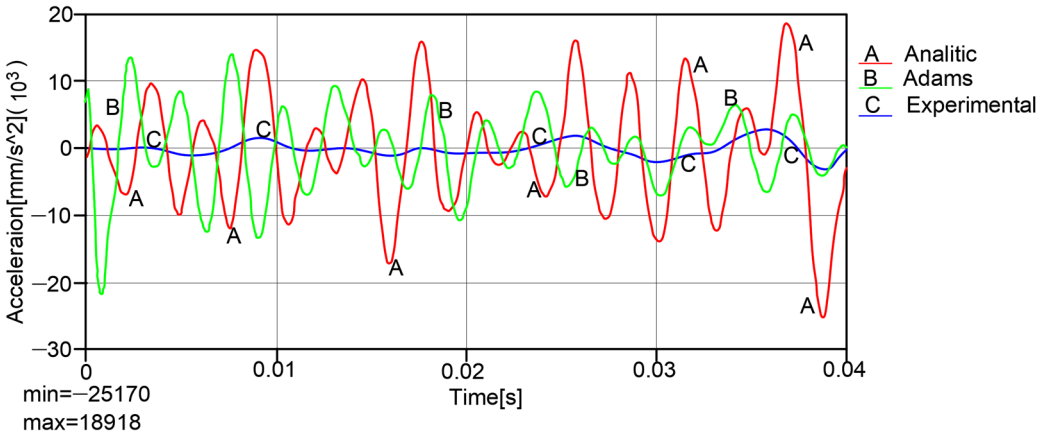


Figure 32. Comparative analysis of connecting rod longitudinal accelerations.

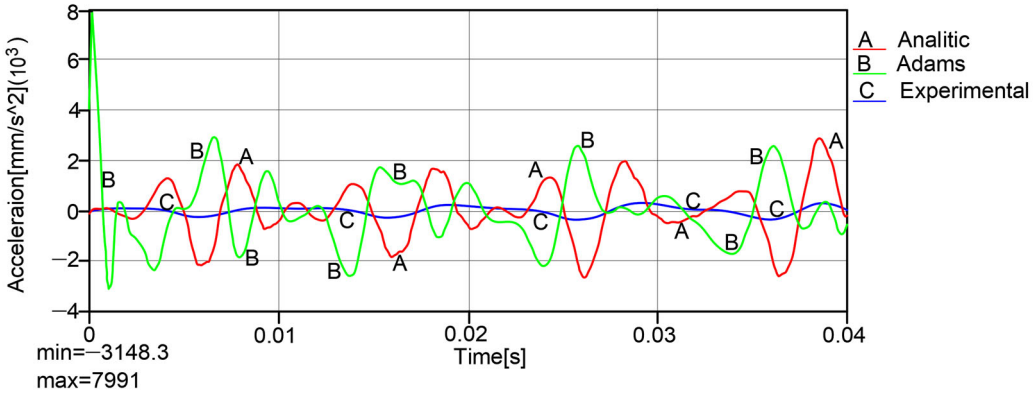


Figure 33. Comparative analysis of connecting rod transversal accelerations.

From Figure 33, we observe that the maximum values of transversal accelerations are equal to 7.9 (m/s^2), with small differences between the mathematical model and virtual prototype. The differences between these and the experimental model can be explained through the fact that the monitoring time interval of the dynamic parameters during tests is much longer than the one used in other processing procedures (25 s instead of 0.04 s).

The extreme longitudinal and transversal values are relatively small in the case of the experimental tests, due to the fact that the experimental tests were performed when the internal combustion engine ran without internal loads and at low rpms. The aim of this was to allow research to be conducted inside of the piston and connecting rod body.

The conclusion is that the numerical results obtained through the three mentioned methods are comparable; thus the mathematical model is correct and can be applied to mechanisms characterized by complex structures, which consist of deformable bodies.

5. Conclusions

The dynamic response of the multibody system consists of two segments: one related to the initial conditions, which damps out quickly, and one related to disturbing forces.

By applying the finite element method, the continuous system was replaced with a discrete system with a finite number of degrees of freedom. The unknowns become nodal displacements $q(t)$ instead of displacement functions $u(x, y, z, t)$.

The system of partial differential equations, specifically the Lame equations from elasticity theory, was converted into a corresponding system of differential equations. The matrices appearing in the general equation of motion were determined by employing the concept of superimposing rigid body motions upon deformable body motions. Rigid body movement was characterized using reference coordinates that specify both the position and orientation of each kinematic link's local reference frame.

In the presented method, the matrices that define the equation of motion ([*M*], [*K*], and [*C*]) include both elastic and rigid deformations. The dynamic components of these matrices result from rigid body motion, while the standard components result from the motion of a deformable body.

In this study, the presented method does not take into account the possible errors from kinematic joints, such as clearances which are present under impact forces. However it is possible to decouple kinematic links and to introduce the corresponding connection forces. The accuracy of the obtained results is influenced by the type and number of finite elements, as well as the method for determining modal forms. This method can be experimental or based on calculations using material properties and the geometric characteristics of elements.

The mathematical models obtained for the dynamic analysis of multibody systems were applied to a crank–connecting rod mechanism used to drive a three-piston inline engine. Each kinematic link was considered as a finite element "beam" type, with two nodes and three degrees of freedom per node, corresponding to the nodal displacement vector. The shape function matrices for axial and transversal displacements, as well as the generalized coordinate vector for the entire assembled system, were determined. For each finite element, the nodal force static and dynamic components, the stiffness matrix, and the damping matrix were determined relative to both the local and global axis systems, using coordinate transformation matrices to move from one reference system to another. The linear, transversal, and angular nodal displacements of the connecting rod in the mechanism were determined using the modal superposition method.

Using the finite element method, both 3D longitudinal and transversal elastic displacements along the connecting rod and 2D displacements at various points in its plane were determined.

To verify the results from the mathematical models, a dynamic analysis was conducted in Adams using multibody system dynamic theory.

The system's motion is driven by the force developed by the gas on the piston head as a result of the gas pressure, which was experimentally determined. The same force was considered in the mathematical models.

A comparative analysis of linear, transversal, and angular nodal displacements showed similar maximum and minimum values, as well as comparable variation curves.

An analysis of the 3D diagrams indicates that the peak longitudinal elastic displacement is 0.003 mm, whereas the maximum transversal elastic displacement is 0.015 mm. At the midpoint of the connecting rod length, the variation curves for the two types of longitudinal and transversal displacements register appropriate values with similar variation shapes. The recorded differences mainly occur since in the dynamic analysis with the Adams program, the engine torque exhibits a jump during startup for a few milliseconds, then stabilizes around 150 [Newtonxmeter].

The matrix approach to the mathematical models allowed for the development of a flexible calculation program with rapid applications for the dynamic analysis of multibody systems with deformable elements.

The experimental analysis allowed for the monitoring of the time and frequency characteristics of kinematic and dynamic parameters, specifically for each of the three

connecting rods in the mechanism (including forces, as well as longitudinal and transversal accelerations). The dynamic response of the three connecting rods was monitored at low speeds and without load on the piston, using a longitudinally sectioned engine.

The presented method can be used for multibody systems where there are large rotations and displacements of the rigid body and small elastic deformation in rapport with a flexible reference system. The finite element displacements of a deformable body were described through a coupled set of coordinate references of the body and others for the nodal displacements. Thus, depending on the finite element type, the effect of large deformations can be considered.

As a final conclusion, the developed method allows us to study, from dynamic viewpoints, the mechanical systems characterized by rapid motions and high rotational speeds of their kinematic links by superimposing rigid body motion with the motion of a deformable body. Meshing into finite elements coupled through nodes leads to complex mathematical models. However, the adopted matrix formalism is a flexible one, which easily allows us to design a general-purpose program for the numerical processing of the developed mathematical models for any mobile mechanical system.

Author Contributions: Conceptualization, N.D. and S.D.; methodology, N.D.; software, A.S.R.; validation, N.D., S.D., and C.C.; formal analysis, C.C.; investigation, N.D.; resources, S.D.; data curation, A.S.R.; writing—original draft preparation, N.D.; writing—review and editing, C.C.; visualization, A.S.R.; supervision, N.D.; project administration, N.D.; funding acquisition, S.D. All authors have read and agreed to the published version of the manuscript.

Funding: This research received no external funding.

Data Availability Statement: Data are available on request to the authors.

Conflicts of Interest: The authors declare no conflicts of interest.

References

1. Piras, G.; Cleghorn, W.L.; Mills, J.K. Dynamic finite—Element analysis of a planar high—Speed, high—Precision parallel manipulator with flexible links. *Mech. Mach. Theory* **2005**, *40*, 849–862. [CrossRef]
2. Cleghorn, W.L.; Fenton, G.; Tabarrok, B. Finite element analysis of high—Speed flexible mechanisms. *Mech. Mach. Theory* **1981**, *16*, 407–424. [CrossRef]
3. Bahgat, B.M.; Willmert, K.D. Finite element vibrational analysis of planar mechanisms. *Mech. Mach. Theory* **1976**, *11*, 47–71. [CrossRef]
4. Rong, B.; Rui, X.T.; Tao, L.; Wang, G.P. Theoretical modeling and numerical solution methods for flexible multibody system dynamics. *Nonlinear Dyn.* **2019**, *98*, 1519–1553. [CrossRef]
5. Song, J.O.; Haug, E.J. Dynamic analysis of planar flexible mechanisms. *Comput. Methods Appl. Mech. Eng.* **1980**, *24*, 359–381. [CrossRef]
6. Vlase, S.; Marin, M.; Itu, C. Gibbs–Appell Equations in Finite Element Analysis of Mechanical Systems with Elements Having Micro—Structure and Voids. *Mathematics* **2024**, *12*, 178. [CrossRef]
7. Scutaru, M.L.; Vlase, S. Two—Dimensional Equivalent Models in the Analysis of a Multibody Elastic System Using the Finite Element Analysis. *Mathematics* **2023**, *11*, 4149. [CrossRef]
8. Korayem, M.H.; Dehkordi, S.F. Motion equations of cooperative multi flexible mobile manipulator via recursive Gibbs—Appell formulation. *Appl. Math. Model.* **2019**, *65*, 443–463. [CrossRef]
9. Wang, Z.; Tian, Q.; Hu, H. Dynamics of Flexible Multibody Systems With Hybrid Uncertain Parameters. *Mech. Mach. Theory* **2018**, *121*, 128–147. [CrossRef]
10. Ren, J.; Zhang, J.; Wei, Q. Dynamic analysis of planar four—Bar mechanism with clearance in microgravity environment. *Nonlinear Dyn.* **2024**, *112*, 15933–15951. [CrossRef]
11. Marques, F.; Roupa, I.; Silva, M.T.; Flores, P.; Lankarani, H.M. Examination and comparison of different methods to model closed loop kinematic chains using Lagrangian formulation with cut joint, clearance joint constraint and elastic joint approaches. *Mech. Mach. Theory* **2021**, *160*, 104294. [CrossRef]
12. Zhang, X.; Erdman, A.G. Dynamic responses of flexible linkage mechanisms with viscoelastic constrained layer damping treatment. *Comput. Struct.* **2001**, *79*, 1265–1274. [CrossRef]

13. Xianmi, Z.; Yunwen, S. Optimal design of flexible mechanisms with frequency constraints. *Mech. Mach. Theory* **1995**, *30*, 131–139. [CrossRef]
14. Shabana, A.A. On the integration of large deformation finite element and multibody system algorithms. In Proceedings of the International Conference on Mechanical Engineering and Mechanics, Halkidiki, Greece, 12–17 June 2005; pp. 63–70.
15. Luo, K.; Liu, C.; Hu, H.Y. Nonlinear static and dynamic analysis of hyper—Elastic thin shells via the absolute nodal coordinate formulation. *Nonlinear Dyn.* **2016**, *85*, 949–971. [CrossRef]
16. Lu, H.J.; Rui, X.T.; Ding, Y.Y.; Chang, Y.; Chen, Y.H.; Ding, J.G.; Zhang, X.P. A hybrid numerical method for vibration analysis of linear multibody systems with flexible components. *Appl. Math. Model.* **2022**, *101*, 748–771. [CrossRef]
17. Ma, W.; Liu, H.; Wang, G.; Xiao, J. An elastodynamic modeling approach based on experimental substructuring for a mobile hybrid robot. *Mech. Mach. Theory* **2025**, *205*, 105892. [CrossRef]
18. Song, N.; Peng, H.; Xu, X.; Wang, G. Modeling and simulation of a planar rigid multibody system with multiple revolute clearance joints based on variational inequality. *Mech. Mach. Theory* **2020**, *154*, 104053. [CrossRef]
19. Sun, D.; Shi, Y.; Zhang, B. Dynamic Analysis of Planar Mechanisms With Fuzzy Joint Clearance and Random Geometry. *ASME J. Mech. Des.* **2019**, *141*, 042301. [CrossRef]
20. Dumitru, N.; Craciunoiu, N.; Geonea, I.; Copilusi, C. Elastodynamic analysis of a mechanism with flexible links. In Proceedings of the World Congress on Engineering, London, UK, 5—7 June 2017; Volume 2, pp. 821–828.
21. Craig, R.R., Jr.; Bampton, M.C. Coupling of substructures for dynamic analyses. *AIAA J.* **1968**, *6*, 1313–1319. [CrossRef]
22. Amirouche, F.M.L. *Computational Methods in Multibody Dynamics*; Prentice—Hall: Englewood Cliffs, NJ, USA, 1992.
23. Kane, T.R.; Likins, P.W.; Levinson, D.A. *Spacecraft Dynamics*; McGraw-Hill: New York, NY, USA, 1983.

Disclaimer/Publisher's Note: The statements, opinions and data contained in all publications are solely those of the individual author(s) and contributor(s) and not of MDPI and/or the editor(s). MDPI and/or the editor(s) disclaim responsibility for any injury to people or property resulting from any ideas, methods, instructions or products referred to in the content.